J. Fluid Mech. (2014), *vol.* 751, *pp.* 627–662. © Cambridge University Press 2014
doi:10.1017/jfm.2014.306

Wall to wall optimal transport

Pedram Hassanzadeh[1,‡], Gregory P. Chini[2] and Charles R. Doering[3,†]

[1]Department of Mechanical Engineering, University of California, Berkeley, CA 94720, USA

[2]Department of Mechanical Engineering, Program in Integrated Applied Mathematics and Center for Fluid Physics, University of New Hampshire, Durham, NH 03824, USA

[3]Department of Mathematics, Department of Physics and Center for the Study of Complex Systems, University of Michigan, Ann Arbor, MI 48109, USA

(Received 22 September 2013; revised 9 April 2014; accepted 24 May 2014;
first published online 24 June 2014)

The calculus of variations is employed to find steady divergence-free velocity fields that maximize transport of a tracer between two parallel walls held at fixed concentration for one of two constraints on flow strength: a fixed value of the kinetic energy (mean square velocity) or a fixed value of the enstrophy (mean square vorticity). The optimizing flows consist of an array of (convection) cells of a particular aspect ratio Γ. We solve the nonlinear Euler–Lagrange equations analytically for weak flows and numerically – as well as via matched asymptotic analysis in the fixed energy case – for strong flows. We report the results in terms of the Nusselt number Nu, a dimensionless measure of the tracer transport, as a function of the Péclet number Pe, a dimensionless measure of the strength of the flow. For both constraints, the maximum transport $Nu_{MAX}(Pe)$ is realized in cells of decreasing aspect ratio $\Gamma_{opt}(Pe)$ as Pe increases. For the fixed energy problem, $Nu_{MAX} \sim Pe$ and $\Gamma_{opt} \sim Pe^{-1/2}$, while for the fixed enstrophy scenario, $Nu_{MAX} \sim Pe^{10/17}$ and $\Gamma_{opt} \sim Pe^{-0.36}$. We interpret our results in the context of buoyancy-driven Rayleigh–Bénard convection problems that satisfy the flow intensity constraints, enabling us to investigate how the transport scalings compare with upper bounds on Nu expressed as a function of the Rayleigh number Ra. For steady convection in porous media, corresponding to the fixed energy problem, we find $Nu_{MAX} \sim Ra$ and $\Gamma_{opt} \sim Ra^{-1/2}$, while for steady convection in a pure fluid layer between stress-free isothermal walls, corresponding to fixed enstrophy transport, $Nu_{MAX} \sim Ra^{5/12}$ and $\Gamma_{opt} \sim Ra^{-1/4}$.

Key words: Bénard convection, convection in porous media, variational methods

1. Introduction

Transport and mixing by incompressible flows are ubiquitous phenomena in science and engineering. In some applications, e.g. cooling or heating, the aim may be to maximize transport of an advected and diffused quantity. In other problems, such as pollutant spills, the goal may be to move a substance from one location to another

† Email address for correspondence: doering@umich.edu
‡ Present address: Centre for the Environment and Department of Earth and Planetary Sciences, Harvard University, Cambridge, MA 02139, USA.

https://doi.org/10.1017/jfm.2014.306 Published online by Cambridge University Press

as quickly as possible while minimizing mixing. In some systems, whether naturally occurring or engineered, the transported quantity is passive, moved by the fluid but not forcing the flow, whereas in other situations, including thermal and compositional convection, it is active and drives its own displacement.

In every case, once the relevant equations of motions are agreed upon, key theoretical challenges include: (*a*) qualitatively understanding the physical mechanisms of transport and mixing in the mathematical model; (*b*) quantitatively estimating the magnitude and/or efficiency of these processes as functions of the initial and boundary conditions, source and sink distributions and/or applied forces; (*c*) determining fundamental limits on the transport and/or mixing effectiveness of relevant classes of fluid flows in terms of rigorous bounds; and (*d*) understanding how such limits might be approached, or even achieved.

The topic of maximal transport has played a significant role in theoretical and mathematical fluid mechanics at least since Malkus (1954) raised the question of limits on heat transfer in thermal convection 60 years ago. Indeed, Malkus' speculation that convective turbulence might optimize heat transport inspired Howard (1963) to derive upper bounds on heat transport in Rayleigh–Bénard convection from the Boussinesq approximation to the Navier–Stokes equations. His approach combined the connection between bulk-averaged convective heat flux and turbulent energy dissipation, a mild statistical hypothesis and a clever variational analysis to produce the first effective rigorous limits on turbulent transport. Howard's variational problem was soon subjected to sophisticated asymptotic analysis by Busse (1969), and was generalized to derive limits on momentum transport in shear flows (Nickerson 1969; Busse 1970), thermal convection in a fluid-saturated porous layer (Busse & Joseph 1972; Gupta & Joseph 1973) and, later, aspects of passive tracer transport in shear-driven turbulence (Krommes & Smith 1987).

An alternative variational formulation for extremes of heat and momentum transport in boundary-driven flows was introduced over two decades ago by Doering & Constantin (1992, 1994, 1996). In some scenarios this so-called 'background method' reproduces the mathematical estimates following from Howard's approach (Kerswell 1998), but it has also produced a steady stream of original results for systems including turbulent precession (Kerswell 1996), shear- and stress-driven flows (Doering, Spiegel & Worthing 2000; Tang, Caulfield & Young 2004; Hagstrom & Doering 2010, 2014), turbulent mixing (Caulfield & Kerswell 2001; Tang, Caulfield & Kerswell 2009) and a variety of buoyancy-driven flows (Siggers, Kerswell & Balmforth 2004; Doering, Otto & Reznikoff 2006; Whitehead & Doering 2011), such as Rayleigh–Bénard convection in a fluid-saturated porous layer (Doering & Constantin 1998; Wen *et al.* 2013).

A distinct mathematical strategy applicable to body-force-driven (rather than boundary-driven) flows was proposed a dozen years ago by Doering & Foias (2002) and subsequently used to produce bounds on the turbulent energy dissipation rate for a variety of Navier–Stokes flows (Doering, Eckhardt & Schumacher 2003; Petrov, Lu & Doering 2005; Cheskidov, Petrov & Doering 2007; Rollin, Dubief & Doering 2011). That approach was also generalized to deduce limits on passive tracer mixing as measured by the suppression of tracer concentration variance (and other norms) in the presence of scalar sources and sinks; see, for example, Thiffeault, Doering & Gibbon (2004), Plasting & Young (2006), Shaw, Thiffeault & Doering (2007) and Okabe *et al.* (2008).

In active transport problems, the maximally transporting 'optimal' flows produced by bounding analyses are normally not solutions of the underlying equations of

https://doi.org/10.1017/jfm.2014.306 Published online by Cambridge University Press

motion for the fluid. The bounding methods mentioned above involve extremizing transport or dissipation over a larger set of flows, a superset of the solutions that share certain features including incompressibility, boundary conditions and a selection of suitably averaged energy, momentum and/or other bulk balances. Of course, the precision of a bound may be questioned if the optimizing flow is not realized as an exact solution of the equations of motion. (The high-Reynolds-number scaling of a dissipation rate bound is known to be sharp, realized by an exact solution of the Navier–Stokes equations, in at least one case; see Doering *et al.* (2000).) Nevertheless, such optimal flows provide insight into the structure of maximally effective modes of transport, whether or not they are naturally realizable.

Several researchers recently formulated some maximal transient mixing models as optimal control problems. The idea here is to determine, from within a specified class of admissible flows, those stirring protocols that extremize an appropriate measure of mixing at a specific instant of time or its rate of change as a function of time; see, for example, D'Alessandro, Dahleh & Mezic (1999), Mathew *et al.* (2007), Cortelezzi, Adrover & Giona (2008), Gubanov & Cortelezzi (2010, 2012) and Lin, Thiffeault & Doering (2011). Constraints on the admissible class of flows include incompressibility and boundary conditions, a limit (of some sort) on flow intensity and possibly other structural restrictions. Although the flows are not required *a priori* to solve any particular physical equations of motion, any such divergence-free velocity field can formally be considered a solution of the incompressible Stokes, Navier–Stokes or even Euler equations satisfying their boundary conditions subjected to suitable body forces. The realizability issue is then an 'engineering' challenge to implement the body forces that generate the desired flow. Again, whether or not it is practical or even possible to design such a system, the optimal flows provide physical insight into the mechanics of mixing, and the rigorous bounds provide a concrete target to strive for.

These three-score years of study serve as the context and provide the inspiration and motivation for the research reported in this paper. As a natural next step along this line of investigation, we address two general and generic questions.

(*a*) What is the maximum rate at which a tracer (a scalar concentration that we will refer to as temperature) can be transported by divergence-free velocity fields satisfying some given boundary conditions and flow intensity constraints?
(*b*) What does the optimizing velocity field look like?

The precise problem we pose is a combination of the continuing challenge to derive sharp bounds on heat transport in Rayleigh–Bénard convection and a precursor to an optimal control approach to transport problems in Navier–Stokes flows. The conditions and constraints considered here are (i) that the flow is confined between two impermeable parallel boundaries and is endowed with a specified root-mean-square speed or vorticity, and (ii) that the concentration of the tracer is constant on each boundary, i.e. the boundaries are isothermal. For simplicity we restrict attention to steady flows in two spatial dimensions. We do not require the incompressible velocity field to satisfy any familiar momentum equation (e.g. for motion driven by the buoyancy force) but only a suitable bulk amplitude constraint which, after the fact, may be interpreted in terms of well-known dissipation–transport balances (e.g. for classical Rayleigh–Bénard convection). Unlike prior approaches to deriving rigorous bounds, however, in this analysis the full advection–diffusion equation for the transported scalar field is enforced as a constraint.

In the next section we present the full formulation of the problem. Subsequently, in §§ 3 and 4, we analyse the problem with, respectively, the fixed energy (mean

https://doi.org/10.1017/jfm.2014.306 Published online by Cambridge University Press

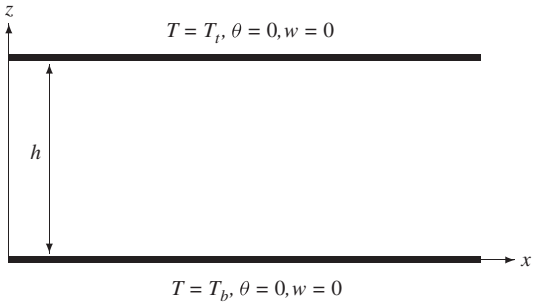


FIGURE 1. Schematic of the configuration. The top and bottom boundaries are impermeable and held at fixed temperatures.

square speed) and fixed enstrophy (mean square vorticity) constraints on stirring strength. We then employ the calculus of variations to maximize the relevant transport, a functional of the flow, subject to the relevant constraints. The nonlinear Euler–Lagrange equations are linearized for weak flows and solved analytically, and for stronger flows we solve the Euler–Lagrange equations using numerical continuation. Exploiting observed symmetries, we solve the Euler–Lagrange equations via matched asymptotic analysis in the fixed energy case. The maximal transport obtained thereby serves as an upper bound for problems that share the boundary conditions and flow intensity constraints. We compare these results for relevant Rayleigh–Bénard problems: convection in a fluid-saturated porous layer (fixed energy) and convection in a Boussinesq fluid with stress-free boundaries (fixed enstrophy). The concluding section, § 5, includes a discussion of future work utilizing this and related approaches to study extreme behaviour in fluid dynamical systems.

2. Mathematical formulation

We focus on heat transport in two dimensions in terms of a temperature field $T(x, z, t)$ satisfying the advection–diffusion equation

$$\dot{T} + \boldsymbol{v} \cdot \boldsymbol{\nabla} T = \kappa \Delta T, \tag{2.1}$$

where $\dot{T} = \partial T/\partial t$, $\Delta = \partial^2/\partial x^2 + \partial^2/\partial z^2$, κ is the (constant) thermal diffusivity of the fluid and $\boldsymbol{v}(x, z, t) = u\hat{\boldsymbol{x}} + w\hat{\boldsymbol{z}}$ is an incompressible flow field, i.e.

$$\boldsymbol{\nabla} \cdot \boldsymbol{v} = 0. \tag{2.2}$$

The geometry of the problem is shown in figure 1. The domain $D = [0, L] \times [0, h]$ is bounded by two parallel impermeable walls held at fixed temperatures. Respecting tradition, we align the walls horizontally in the x direction separated by distance h in the vertical z direction. All system variables are periodic in the x direction with horizontal period L.

We consider velocity fields that have either fixed mean squared speed

$$U^2 = \frac{1}{hL} \int_D |\boldsymbol{v}|^2 \, \mathrm{d}x \, \mathrm{d}z \tag{2.3}$$

https://doi.org/10.1017/jfm.2014.306 Published online by Cambridge University Press

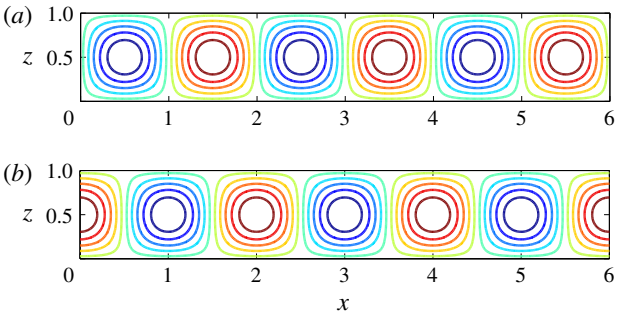


FIGURE 2. (Colour online) Optimal flow field in the small-*Pe* limit for the fixed energy problem: (*a*) streamlines ψ; (*b*) temperature θ.

or fixed enstrophy density

$$\Omega^2 = \frac{1}{hL}\int_D |\boldsymbol{\omega}|^2 \,\mathrm{d}x\,\mathrm{d}z = \frac{1}{hL}\int_D |\boldsymbol{\nabla v}|^2 \,\mathrm{d}x\,\mathrm{d}z, \tag{2.4}$$

where $\boldsymbol{\omega} = \boldsymbol{\nabla} \times \boldsymbol{v}$ is the vorticity and $|\boldsymbol{\nabla v}|^2 = \boldsymbol{\nabla v} : \boldsymbol{\nabla v}$. The second equality in (2.4) follows for many boundary conditions on impermeable horizontal boundaries, including no-slip and stress-free conditions. (By 'stress-free' we mean homogeneous Neumann boundary conditions on the tangential velocity component, i.e. $\partial u/\partial z = 0$, corresponding to stress-free boundaries for Newtonian fluids.) The physical significance of the second expression is that, when multiplied by viscosity, it yields the viscous energy dissipation rate for Newtonian fluids in these domains. Hence the enstrophy constraint is natural to consider in situations where a power budget limits the strength of the flow in a viscous fluid.

We non-dimensionalize the system using the spacing between the walls, h, and the diffusion time scale, h^2/κ. The dimensionless temperature is naturally $(T - T_t)/(T_b - T_t)$, taking values 1 and 0 on the bottom and top boundaries. The (dimensionless) Péclet number *Pe*, which measures the relative strength of the flow, is the ratio of the diffusive time scale to the advective time scale (i.e. a measure of the strength of advection relative to diffusion). For the problem with fixed energy we define

$$Pe \equiv \frac{Uh}{\kappa}, \tag{2.5}$$

and for the problem with fixed enstrophy we take

$$Pe \equiv \frac{\Omega h^2}{\kappa}. \tag{2.6}$$

We also define the aspect ratio

$$\Gamma \equiv \frac{L}{2h}, \tag{2.7}$$

which is the normalized width of a single convection cell associated with the optimal flow (see, e.g., figure 2). In the absence of advection (when $\boldsymbol{v} = 0$) the transport is purely conductive with steady dimensionless temperature field $1 - z$, so we define the dimensionless temperature deviation variable $\theta \equiv (T - T_t)/(T_b - T_t) - 1 + z$,

https://doi.org/10.1017/jfm.2014.306 Published online by Cambridge University Press

which vanishes on the boundaries. Hereafter all variables (i.e. $\boldsymbol{v}$, T, θ, x, z and t) are dimensionless.

Non-dimensionalizing (2.1) and (2.2) and the boundary conditions yields

$$\dot{\theta} + \boldsymbol{v} \cdot \boldsymbol{\nabla}\theta = \Delta\theta + w, \tag{2.8}$$

$$\boldsymbol{\nabla} \cdot \boldsymbol{v} = 0, \tag{2.9}$$

$$\theta(x, 0, t) = \theta(x, 1, t) = 0, \tag{2.10}$$

$$w(x, 0, t) = w(x, 1, t) = 0. \tag{2.11}$$

Define the long time–space average by angle brackets $\langle\cdot\rangle$, as follows:

$$\langle \boldsymbol{a}(x, z, t)\rangle \equiv \lim_{t\to\infty} \frac{1}{t} \int_0^t \left\{ \frac{1}{2\Gamma} \int_D \boldsymbol{a}(x, z, s)\, \mathrm{d}x\, \mathrm{d}z \right\} \mathrm{d}s. \tag{2.12}$$

The fixed energy constraint (2.3) is then

$$Pe^2 = \left\langle |\boldsymbol{v}|^2 \right\rangle, \tag{2.13}$$

while the fixed enstrophy constraint (2.4) is

$$Pe^2 = \left\langle |\boldsymbol{\nabla}\boldsymbol{v}|^2 \right\rangle. \tag{2.14}$$

The Nusselt number Nu measures the scalar transport by advection and is defined as the ratio of the total flux in the presence of advection to the heat flux by pure conduction. We are interested in the vertical transport between horizontal walls, so

$$Nu = 1 + \langle wT\rangle = 1 + \langle w\theta\rangle. \tag{2.15}$$

Note that $\langle w f(\cdot)\rangle = 0$ for any $f(z)$ as a result of incompressibility and the boundary conditions.

2.1. *Objective*

With the strength of advection gauged by Pe, the geometry of the flow parameterized by Γ and the strength of transport measured by Nu as defined above, we are now in a position to fully formulate the task at hand.

Step 1. Search over all steady divergence-free velocity fields $\boldsymbol{v}$ with given (Pe, Γ) that satisfy (2.11) to find the maximum possible value of Nu in (2.15), noting that $\boldsymbol{v}$, (2.8) and (2.10) uniquely determine a steady-state $\theta(x, z)$. This maximum is denoted by

$$Nu_{max}(Pe, \Gamma) \equiv \sup_{\boldsymbol{v}} \{Nu(\boldsymbol{v})\}. \tag{2.16}$$

Step 2. For the same Pe, step 1 may be repeated for various values of Γ. For each value of Pe, the largest value of $Nu_{max}(Pe, \Gamma)$ will be called

$$Nu_{MAX}(Pe) \equiv \sup_{\Gamma} \{Nu_{max}(Pe, \Gamma)\}. \tag{2.17}$$

Step 3. For each value of Pe, the Γ from step 2 that realizes Nu_{MAX} is dubbed the optimal aspect ratio and denoted by $\Gamma_{opt}(Pe)$; that is, $Nu_{MAX}(Pe) = Nu_{max}(Pe, \Gamma_{opt}(Pe))$.

The time (in)dependence of the flow merits further discussion. The effect of unsteadiness on optimal transport is not fully understood, and whether a time-dependent flow can transport more than a steady flow (with the same amount of energy or enstrophy) remains an open question. Of course, the question can be answered by performing the optimization in step 1 over both space and time, i.e. by considering $\boldsymbol{v} = \boldsymbol{v}(x, z, t)$. Such an analysis is a problem of optimal control theory and is left for the future. Here we focus on steady flows (i.e. $\boldsymbol{v} = \boldsymbol{v}(x, z)$) and use calculus of variations to carry out step 1.

https://doi.org/10.1017/jfm.2014.306 Published online by Cambridge University Press

3. Optimal transport with fixed energy

The steady-state fixed energy system, (2.8)–(2.11) and (2.13), is

$$\boldsymbol{v}\cdot\boldsymbol{\nabla}\theta = \Delta\theta + w, \tag{3.1}$$
$$\boldsymbol{\nabla}\cdot\boldsymbol{v} = 0, \tag{3.2}$$
$$Pe^2 = \left\langle |\boldsymbol{v}|^2 \right\rangle, \tag{3.3}$$
$$\theta(x,0) = \theta(x,1) = 0, \tag{3.4}$$
$$w(x,0) = w(x,1) = 0. \tag{3.5}$$

Before solving this system, we note that a simple analysis yields a rigorous *a priori* upper bound on Nu. Starting from (2.15), recalling the Cauchy–Schwarz inequality and remembering that the maximum principle assures $0 \leqslant T \leqslant 1$ so that $|T - 1/2| \leqslant 1/2$,

$$\begin{aligned} Nu &= 1 + \langle wT \rangle = 1 + \langle w(T-1/2) \rangle \\ &\leqslant 1 + \left\langle w^2 \right\rangle^{1/2} \left\langle (T-1/2)^2 \right\rangle^{1/2} \\ &\leqslant 1 + \frac{\left\langle |\boldsymbol{v}|^2 \right\rangle^{1/2}}{2} = 1 + \frac{Pe}{2}. \end{aligned} \tag{3.6}$$

3.1. *Variational formulation for steady flows*

The variational problem to maximize $Nu = 1 + \langle \theta w \rangle$ given constraints (3.1)–(3.3) and boundary conditions (3.4) and (3.5) is to extremize the functional

$$\mathcal{F} = \left\langle w\theta - \phi(x,z)\left(\boldsymbol{v}\cdot\boldsymbol{\nabla}\theta - \Delta\theta - w\right) + p(x,z)\left(\boldsymbol{\nabla}\cdot\boldsymbol{v}\right) - \frac{\mu}{2}\left(|\boldsymbol{v}|^2 - Pe^2\right) \right\rangle \tag{3.7}$$

where $\phi(x,z)$, $p(x,z)$ and μ are Lagrange multipliers; ϕ and p are functions of x and z to enforce the differential constraints (3.1) and (3.2) pointwise in space, while μ is a real number. The Euler–Lagrange equations are

$$0 = \frac{\delta\mathcal{F}}{\delta\boldsymbol{v}} = (\theta+\phi)\,\hat{\boldsymbol{z}} + \theta\,\boldsymbol{\nabla}\phi - \boldsymbol{\nabla}p - \mu\boldsymbol{v}, \tag{3.8}$$
$$0 = \frac{\delta\mathcal{F}}{\delta\theta} = \boldsymbol{v}\cdot\boldsymbol{\nabla}\phi + \Delta\phi + w, \tag{3.9}$$
$$0 = \frac{\delta\mathcal{F}}{\delta\phi} = -\boldsymbol{v}\cdot\boldsymbol{\nabla}\theta + \Delta\theta + w, \tag{3.10}$$
$$0 = \frac{\delta\mathcal{F}}{\delta p} = \boldsymbol{\nabla}\cdot\boldsymbol{v}, \tag{3.11}$$
$$0 = \frac{\partial\mathcal{F}}{\partial\mu} = \frac{1}{2}\left(Pe^2 - \left\langle |\boldsymbol{v}|^2 \right\rangle\right). \tag{3.12}$$

In deriving (3.9), the natural boundary conditions that ϕ vanishes at $z = 0$ and $z = 1$ were employed to eliminate a surface term arising from the integration by parts of $\phi\Delta\theta$. Therefore, the boundary conditions accompanying these partial differential equations are

$$w(x,0) = w(x,1) = 0, \tag{3.13}$$
$$\theta(x,0) = \theta(x,1) = 0, \tag{3.14}$$
$$\phi(x,0) = \phi(x,1) = 0. \tag{3.15}$$

Note that the $+\theta\boldsymbol{\nabla}\phi$ term in (3.8) is equivalent to $-\phi\boldsymbol{\nabla}\theta$, the difference being a perfect gradient that can be absorbed into $\boldsymbol{\nabla}p$.

https://doi.org/10.1017/jfm.2014.306 Published online by Cambridge University Press

Equations (3.8) and (3.10)–(3.11) exhibit certain similarities to those governing steady Rayleigh–Bénard convection in a fluid-saturated porous layer at infinite Prandtl–Darcy number (see, e.g., Doering & Constantin 1998). But here an extra scalar, the Lagrange multiplier or 'adjoint' field ϕ, enters the problem. This resemblance, which will also be observed in the linear analysis in the next subsection, will be discussed further in § 3.5.

3.2. *The limit of small Pe: asymptotic solution*

In the limit of small *Pe*, the flow field $|\boldsymbol{v}| \ll 1$ (at least in the L^2 sense), which, along with (3.9), (3.10) and the maximum principle, implies that $|\theta| \ll 1$ and $|\phi| \ll 1$. Therefore, in this limit we can linearize equations (3.8)–(3.10) to obtain the system

$$\mu\,\boldsymbol{v} + \boldsymbol{\nabla} p = (\theta + \phi)\,\hat{\boldsymbol{z}}, \tag{3.16}$$

$$\Delta\phi + w = 0, \tag{3.17}$$

$$\Delta\theta + w = 0, \tag{3.18}$$

$$\boldsymbol{\nabla}\cdot\boldsymbol{v} = 0. \tag{3.19}$$

Subtracting (3.18) from (3.17) and using (3.14) and (3.15) then yields $\theta = \phi$. Taking the z-component of the double-curl of (3.16) and using (3.19), we deduce that

$$\mu\,\Delta w = 2\,\theta_{xx} \tag{3.20}$$

where, as usual, subscript x indicates the partial derivative with respect to x.

Equations (3.18)–(3.20) and the boundary conditions (3.13) and (3.14) can be solved analytically in this small-*Pe* limit. Indeed, upon Fourier transforming in the x direction, (3.18) and (3.20) become

$$(\mathrm{D}_z^2 - k^2)\,\hat{\theta}_k(z) + \hat{w}_k(z) = 0, \tag{3.21}$$

$$\mu(\mathrm{D}_z^2 - k^2)\,\hat{w}_k(z) + 2k^2\,\hat{\theta}_k(z) = 0, \tag{3.22}$$

where $\mathrm{D}_z = \mathrm{d}/\mathrm{d}z$ and $\hat{w}_k(z)$ and $\hat{\theta}_k(z)$ are the Fourier coefficients of w and θ with horizontal (dimensionless) wavenumber $k \equiv \pi/\Gamma$. The solution is

$$\hat{w}_k(z) = A_k \sin(m\pi z), \tag{3.23}$$

$$\hat{\theta}_k(z) = B_k \sin(m\pi z), \tag{3.24}$$

where m is the vertical (dimensionless) wavenumber and the coefficients A_k and B_k are still undetermined. Substituting into (3.21) and (3.22) gives

$$\mu = (2\,k^2)/(m^2\pi^2 + k^2)^2, \tag{3.25}$$

$$A_k = (m^2\pi^2 + k^2)\,B_k. \tag{3.26}$$

Using (3.19), we obtain

$$\hat{u}_k(z) = \mathrm{i}\frac{m\pi}{k}\,A_k \cos(m\pi z). \tag{3.27}$$

Substituting (3.27) and (3.23) into (3.12) yields

$$\left\langle |\boldsymbol{v}|^2 \right\rangle = \left(A_k^2 + \frac{m^2\pi^2}{k^2}A_k^2\right) = Pe^2 \implies A_k = \frac{k}{(m^2\pi^2 + k^2)^{1/2}}\,Pe, \tag{3.28}$$

https://doi.org/10.1017/jfm.2014.306 Published online by Cambridge University Press

which, along with (3.26), gives

$$B_k = \frac{k}{(m^2\pi^2 + k^2)^{3/2}}\, Pe. \tag{3.29}$$

Knowing A_k and B_k, Nu is obtained from (2.15) as

$$Nu = 1 + A_k B_k = 1 + \frac{k^2}{(m^2\pi^2 + k^2)^2}\, Pe^2. \tag{3.30}$$

Then, for a given parameter set (Pe, $\Gamma = \pi/k$), Nu is maximized at $m = 1$. As a result, using the notation defined in § 2.1,

$$Nu_{max}(Pe, \Gamma) = 1 + \frac{\Gamma^2}{\pi^2(\Gamma^2 + 1)^2}\, Pe^2. \tag{3.31}$$

The largest value of $Nu_{max}(Pe, \Gamma)$, i.e. Nu_{MAX}, is achieved at $\Gamma_{opt} = 1$:

$$Nu_{MAX}(Pe) = 1 + \frac{Pe^2}{4\pi^2}. \tag{3.32}$$

Note that $(k, m) = (\pi, 1)$ corresponds to the maximum value of $\mu = 1/(2\pi)^2$; see (3.25).

Therefore, in the limit of small Pe (i.e. large μ), the maximum transport is realized by an array of square convection cells (rolls) with optimal aspect ratio $\Gamma_{opt} = 1$. Figure 2 shows this flow field where the square convection cells are clearly seen. This solution is identical to the first unstable mode at onset for Rayleigh–Bénard convection in a fluid-saturated porous media (Doering & Constantin 1998). Additionally, we note (and discuss further in § 3.5) that the factor $4\pi^2$ arising in (3.32) is the critical Ra for the instability.

3.3. *Small to large Pe: numerical solution*

For $Pe > O(1)$, the full nonlinear system (3.8)–(3.11) must be solved. Defining the stream function ψ by $u = \partial\psi/\partial z$ and $w = -\partial\psi/\partial x$, (3.8)–(3.11) reduce to

$$\mathrm{J}(\theta, \phi) + \mu\,\Delta\psi + (\theta + \phi)_x = 0, \tag{3.33}$$

$$-\mathrm{J}(\psi, \phi) + \Delta\phi - \psi_x = 0, \tag{3.34}$$

$$-\mathrm{J}(\psi, \theta) - \Delta\theta + \psi_x = 0, \tag{3.35}$$

where $\mathrm{J}(a, b) = (\partial a/\partial x)(\partial b/\partial z) - (\partial a/\partial z)(\partial b/\partial x)$. The boundary conditions (3.13)–(3.15) become

$$\psi(x, 0) = \psi(x, 1) = 0, \tag{3.36}$$

$$\theta(x, 0) = \theta(x, 1) = 0, \tag{3.37}$$

$$\phi(x, 0) = \phi(x, 1) = 0. \tag{3.38}$$

These equations and boundary conditions imply an interesting symmetry between θ and ϕ that will be exposed in the numerical results and exploited later to obtain asymptotic solutions for large Pe.

https://doi.org/10.1017/jfm.2014.306 Published online by Cambridge University Press

3.3.1. *Numerical continuation*

Numerical continuation is a strategy to systematically trace a branch of solutions starting from an initial iterate (Boyd 2001, appendix D). In the problem considered here, the solutions are known analytically in the limit of small Pe (i.e. large μ) for given values of Γ (see § 3.2). These solutions provide suitable initial guesses for solutions at larger values of Pe (i.e. smaller μ), which are computed numerically according to the following continuation algorithm.

(i) Start from the analytical solution for large μ for a given value of Γ.

(ii) Incrementally reduce μ such that, at iteration $N+1$, μ^{N+1} is set to be 0.1–5 % smaller than μ^N. Use the solution at iteration N (with μ^N) as the initial guess to iteratively compute the new solution at iteration $N+1$ (with μ^{N+1}).

(iii) Using the converged solution from step (ii), calculate $Pe(\mu^{N+1}, \Gamma)$ and $Nu_{max}(\mu^{N+1}, \Gamma)$ from the relations

$$Pe^2 = \langle \psi_x^2 + \psi_z^2 \rangle, \tag{3.39}$$

$$Nu_{max} = 1 - \langle \psi_x \theta \rangle. \tag{3.40}$$

(iv) Repeat steps (ii) and (iii), reducing μ (and increasing Pe) by several orders of magnitude.

(v) Repeat steps (i)–(iv) for a variety of values of Γ.

This procedure produces $Nu_{max}(Pe, \Gamma)$ for a wide range of Pe and Γ. Note that in step (i) the vertical wavenumber m must be chosen for the linear solution. Empirically, we find that Nu_{MAX} always emerges from solutions continued from linear solutions with $m = 1$. Therefore, for most cases we set $m = 1$, although cases with $m = 2$ and linearly superposed solutions with different values of m were also studied (see § 3.3.3). The percentage reduction of μ in step (ii) depends on the degree of nonlinearity of the problem; not unexpectedly, μ must be varied more slowly as Pe increases.

3.3.2. *Numerical method*

In this section we present details of the iterative numerical method used in step (ii) of the continuation algorithm. Specifically, we use a Newton–Kantorovich iteration scheme (Boyd 2001, appendix C) with a pseudospectral Chebyshev collocation method (Boyd 2001; Trefethen 2001) to solve (3.33)–(3.35). Instead of solving these equations in a large horizontally periodic domain including multiple cells (such as that shown in figure 2*a*), we choose the computational domain to include only a single cell (figure 3). This unicellular approach has been successfully used to study other, related problems, including Rayleigh–Bénard convection in pure fluids (Chini & Cox 2009) and in porous media (Corson 2011). In this configuration, symmetry boundary conditions are imposed on the vertical sides of the domain at $x = \pm\Gamma/2$. Note that in the computational domain, the horizontal walls are located at $z = \pm 0.5$ (rather than at $z = 0, 1$ as before) for convenience since Chebyshev polynomials are employed.

The Newton–Kantorovich method used in step (ii) of the continuation algorithm (§ 3.3.1) is implemented as follows. The known solution at the Nth iterate, $(\psi^N, \theta^N, \phi^N)$, is used as a first guess to iteratively approximate the true solution at the $(N+1)$th iteration, $(\psi^{N+1}, \theta^{N+1}, \phi^{N+1})$. In what follows, '$\delta$' of any quantity means the difference between its values at iterations $N+1$ and N. By Taylor expanding (3.33)–(3.35) about $(\psi^N, \theta^N, \phi^N)$ and neglecting higher-order terms, we obtain the system of three linear differential equations (A 10)–(A 12) given in appendix A. Applying a pseudospectral

https://doi.org/10.1017/jfm.2014.306 Published online by Cambridge University Press

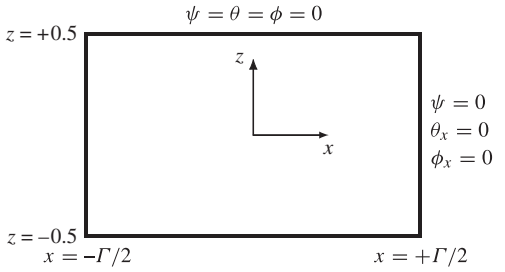


FIGURE 3. The fixed energy problem: the geometry and boundary conditions of the computational domain corresponding to a single two-dimensional (convection) cell. Boundary conditions on the bottom (left) boundary are the same as on the top (right) boundary.

Chebyshev collocation method in both the x and z directions yields the following linear matrix equation:

$$\begin{bmatrix} \mu\Delta & (\boldsymbol{I}+\boldsymbol{\phi}_z^N)\boldsymbol{D}_x - \boldsymbol{\phi}_x^N\boldsymbol{D}_z & (\boldsymbol{I}-\boldsymbol{\theta}_z^N)\boldsymbol{D}_x + \boldsymbol{\theta}_x^N\boldsymbol{D}_z \\ -(\boldsymbol{I}-\boldsymbol{\theta}_z^N)\boldsymbol{D}_x - \boldsymbol{\theta}_x^N\boldsymbol{D}_z & \Delta - \boldsymbol{\psi}_z^N\boldsymbol{D}_x + \boldsymbol{\psi}_x^N\boldsymbol{D}_z & \boldsymbol{O} \\ -(\boldsymbol{I}+\boldsymbol{\phi}_z^N)\boldsymbol{D}_x + \boldsymbol{\phi}_x^N\boldsymbol{D}_z & \boldsymbol{O} & \Delta + \boldsymbol{\psi}_z^N\boldsymbol{D}_x - \boldsymbol{\psi}_x^N\boldsymbol{D}_z \end{bmatrix} \begin{bmatrix} \delta\boldsymbol{\psi} \\ \delta\boldsymbol{\theta} \\ \delta\boldsymbol{\phi} \end{bmatrix} = \begin{bmatrix} -\mu\Delta\boldsymbol{\psi}^N - (\boldsymbol{I}+\boldsymbol{\phi}_z^N)\boldsymbol{\theta}_x^N - (\boldsymbol{I}-\boldsymbol{\theta}_z^N)\boldsymbol{\phi}_x^N \\ -\Delta\boldsymbol{\theta}^N + (\boldsymbol{I}-\boldsymbol{\theta}_z^N)\boldsymbol{\psi}_x^N + \boldsymbol{\psi}_z^N\boldsymbol{\theta}_x^N \\ -\Delta\boldsymbol{\phi}^N + (\boldsymbol{I}+\boldsymbol{\phi}_z^N)\boldsymbol{\psi}_x^N - \boldsymbol{\psi}_z^N\boldsymbol{\phi}_x^N \end{bmatrix}. \tag{3.41}$$

Here $\boldsymbol{I}$ and $\boldsymbol{O}$ are $M^2 \times M^2$ identity and zero matrices, respectively, where M is the number of collocation grid points; $\boldsymbol{D}_x$ and $\boldsymbol{D}_z$ are the x and z differentiation matrices, and $\Delta = \boldsymbol{D}_{xx} + \boldsymbol{D}_{zz}$. These $M^2 \times M^2$ matrices are constructed using tensor products (also known as Kronecker products), as described in detail in Trefethen (2001). The vectors $\boldsymbol{\psi}$, $\boldsymbol{\theta}$ and $\boldsymbol{\phi}$ are of length M^2. The boundary conditions are implemented by modifying the rows corresponding to the boundary grid points in the coefficient matrix and the right-hand side matrix in (3.41).

A MATLAB code was developed to construct the elements of the matrices in (3.41) and to solve the linear algebraic system by direct matrix inversion. Once $\delta\boldsymbol{\psi}$, $\delta\boldsymbol{\theta}$ and $\delta\boldsymbol{\phi}$ are calculated, the solution is updated by setting $(\cdot)^{N+1} = (\cdot)^N + \delta(\cdot)$. The iterations stop when $\delta(\cdot)/\|(\cdot)\|_\infty \leqslant 10^{-10}$ for all three variables $\boldsymbol{\psi}$, $\boldsymbol{\theta}$ and $\boldsymbol{\phi}$. Finally, Clenshaw–Curtis quadrature (Trefethen 2001) is used for all spatial integrations, for example to calculate Pe^2 from (3.39) and Nu_{max} from (3.40).

3.3.3. *Numerical results*

The results presented here were obtained using $M = 61$ or 91. The iterative solution always converged in fewer than six iterations. Figure 4 shows ψ and θ for $\Gamma = 1$ and increasing values of Pe. The flow shown in figure 4(*a*,*b*) is still in the linear regime. The bulk flow structure changes and boundary layers emerge in both ψ and θ as Pe increases (figure 4*c*–*f*).

Figure 5 plots $Nu_{max}(Pe, \Gamma)$ for several values of Γ. This figure exhibits a number of interesting features. Firstly, Nu_{max} agrees with (3.31) in the limit of small Pe, which serves to some extent as a benchmark for the code. Moreover, the absolute upper bound (3.6) quantitatively overestimates the maximum possible high-Péclet-number

https://doi.org/10.1017/jfm.2014.306 Published online by Cambridge University Press

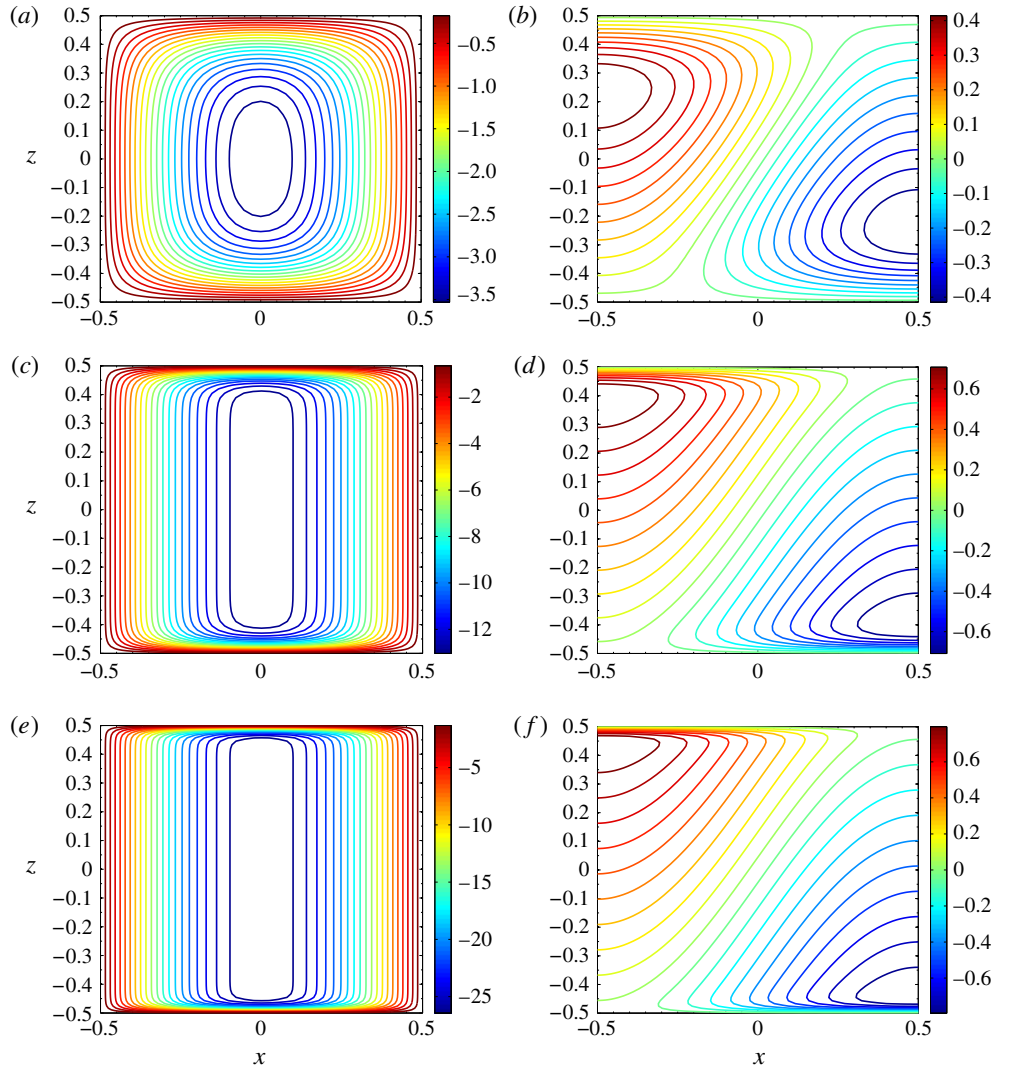


FIGURE 4. (Colour online) Evolution of the flow fields with increasing Pe for the case where $\Gamma = 1$. (*a*,*c*,*e*) show ψ and (*b*,*d*,*f*) show θ. (*a*,*b*) $Pe = 10.0$, $Nu_{max} = 2.4$; (*c*,*d*) $Pe = 59.4$, $Nu_{max} = 9.7$; (*e*,*f*) $Pe = 161.3$, $Nu_{max} = 20.7$. The resolution is 61^2.

heat transport by only an $O(1)$ factor: it captures the correct high-Péclet-number linear scaling. It also shows that $Nu_{MAX}(Pe)$ is obtained from solutions continued from linear solutions with $m = 1$. This is not unexpected, as flows with $m > 1$ include horizontal transport in the bulk far from the boundaries, which evidently is not an efficient use of the available energy. (Indeed, we computed several cases with $m > 1$ as well as a few cases continuing from superposed solutions of two m values, of which only one case is shown in figure 5, and they all confirmed this conclusion.)

Figure 5 also suggests that Nu_{max} scales as $K(\Gamma)\,Pe^{2/3}$ as Pe increases, and that Nu_{MAX} is obtained by flows with smaller Γ as Pe increases. The ensemble of Nu_{max} plotted against Pe for different values of Γ forms an envelope that determines Nu_{MAX}, and the numerical results suggest that $Nu_{MAX} \to C\,Pe$ where C is an absolute

https://doi.org/10.1017/jfm.2014.306 Published online by Cambridge University Press

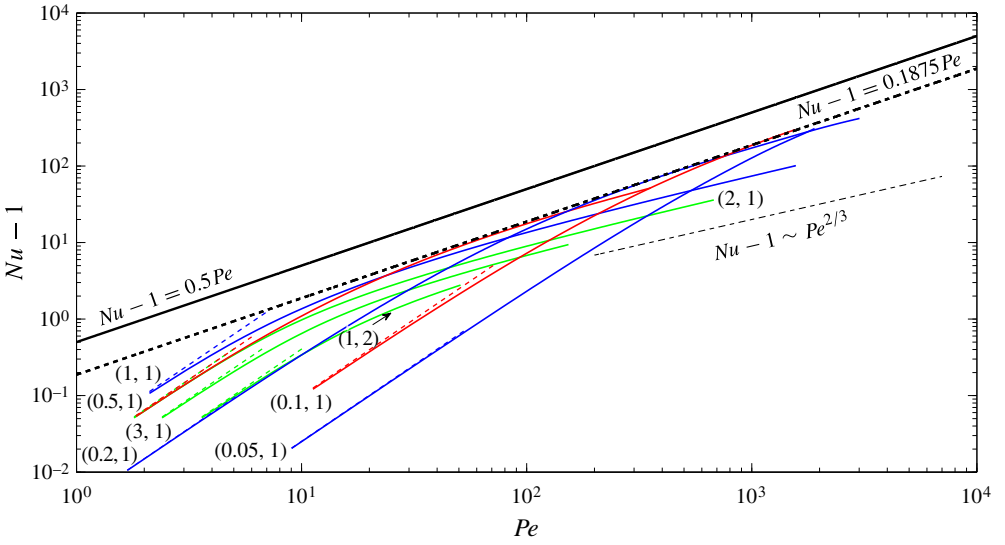


FIGURE 5. (Colour online) The numerically obtained Nu_{max} as a function of Pe for various values of Γ (non-black lines). The labels show (Γ, m). For each case, the (short) dashed line of the same colour, visible in most cases, shows the analytical Nu_{max} given in (3.31) in the small-Pe limit. The thick black solid line represents the absolute upper bound (3.6), and the thick black dashed line shows the analytically obtained Nu_{MAX} given in (3.93), which is derived in the large-Pe limit. The thin black dashed line indicates the $Pe^{2/3}$ slope. Cases with $\Gamma > 1$ or $m > 1$ (green lines) do not produce Nu_{MAX}. All the results shown here have resolution $M = 61$. Using a higher resolution, $M = 91$, results in negligible changes to the plot.

constant prefactor. The prefactors $K(\Gamma)$ and C can, of course, be determined from the numerical results, but this proves to be unnecessary because, guided by the numerics, we are able to obtain asymptotic solutions of (3.33)–(3.35), and hence analytical expressions for Nu_{max}, Nu_{MAX} and Γ_{opt}, in the limit of large Pe in § 3.4. (The analytically derived Nu_{MAX}, given in (3.93), is also plotted in figure 5 and is seen to agree very well with the envelope produced by the numerical results.)

3.4. *The large-Pe asymptotic solution*

The high-Pe (small-μ) numerical solutions plotted in figure 6 (and in figure 2.7 of Hassanzadeh 2012) display some striking features: ψ is nearly independent of z in the bulk and depends on x as $\cos(\pi x/\Gamma)$ in both the bulk and the boundary layers. Also, while θ and ϕ do not have such simple structure in the bulk or boundary layers, the variables

$$\xi(x, z) \equiv \phi(x, z) + \theta(x, z), \tag{3.42}$$

$$\eta(x, z) \equiv \theta(x, z) - \phi(x, z) \tag{3.43}$$

do: ξ (like ψ) is nearly independent of z except close to the top and bottom boundaries, and η is a function of only z everywhere (see figure 6). This observation suggests formulating equations for (ψ, ξ, η) and using matched asymptotic analysis to solve the resulting equations in the large-Pe limit.

https://doi.org/10.1017/jfm.2014.306 Published online by Cambridge University Press

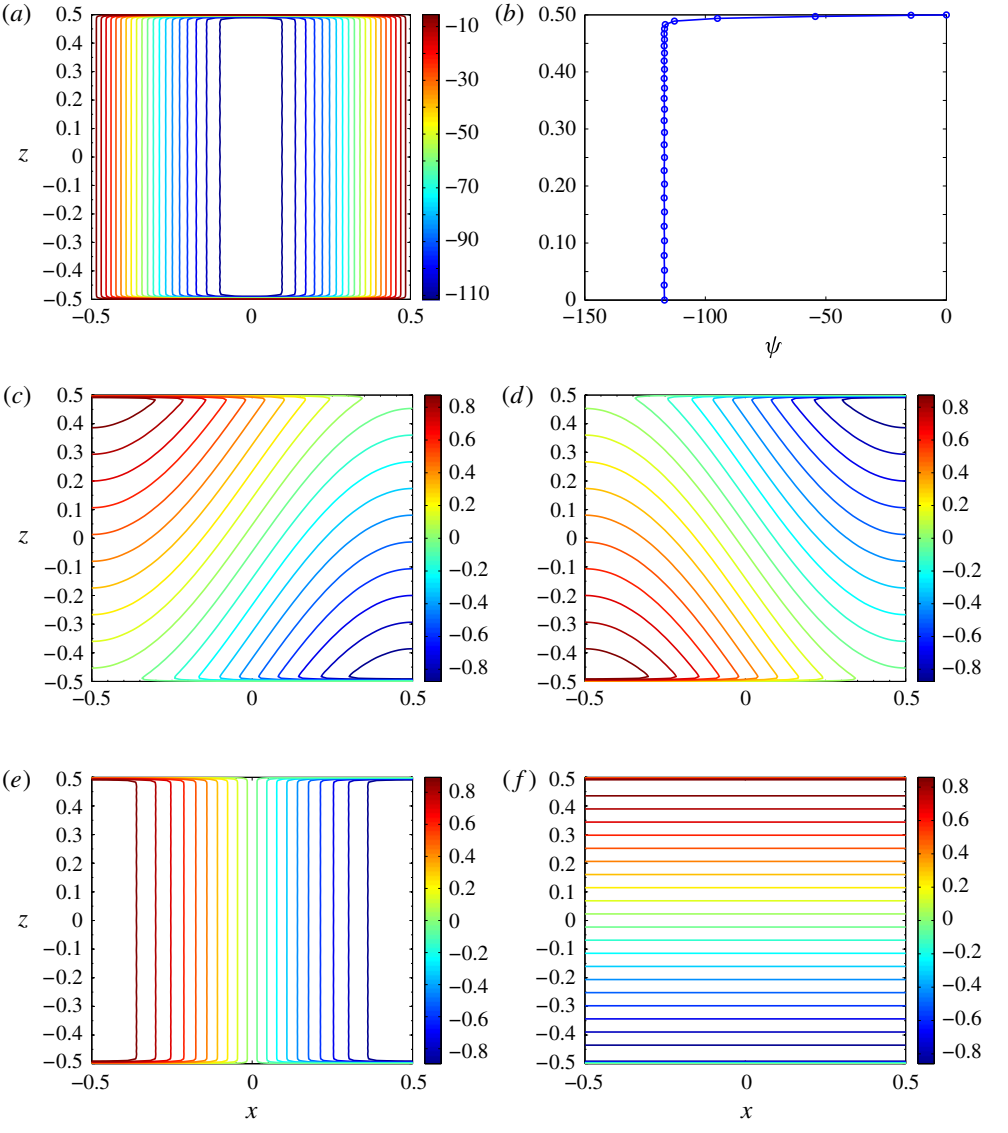


FIGURE 6. (Colour online) Flow field for $\Gamma = 1$, $\mu = 3.557 \times 10^{-5}$, $Pe = 1320.5$ and $Nu_{max} = 90.7$: (*a*) ψ; (*b*) ψ along $x = 0$; (*c*) θ; (*d*) ϕ; (*e*) $\xi \equiv \theta + \phi$; (*f*) $\eta \equiv \theta - \phi$. The resolution is 61^2.

Equations (3.33)–(3.35) imply that the equations for ψ, ξ and η are

$$-\mathrm{J}(\xi, \eta) + 2\mu\Delta\psi + 2\xi_x = 0, \tag{3.44}$$

$$\mathrm{J}(\psi, \xi) + \Delta\eta = 0, \tag{3.45}$$

$$\mathrm{J}(\psi, \eta) + \Delta\xi - 2\psi_x = 0. \tag{3.46}$$

The computational results suggest the ansatzen

$$\psi = \bar{\psi}(x)\, A\left(\frac{1/2 + z}{\delta}\right) A\left(\frac{1/2 - z}{\delta}\right), \tag{3.47}$$

https://doi.org/10.1017/jfm.2014.306 Published online by Cambridge University Press

$$\xi = \bar{\xi}(x)\, B\left(\frac{1/2+z}{\delta}\right) B\left(\frac{1/2-z}{\delta}\right), \tag{3.48}$$

$$\eta = \bar{\eta}(z)\, C\left(\frac{1/2+z}{\delta}\right) C\left(\frac{1/2-z}{\delta}\right), \tag{3.49}$$

where δ denotes the boundary layer thickness. (We introduce a single boundary layer scale here; we originally allowed for three independent boundary layer thicknesses but later deduced that they are, in fact, identical; see Hassanzadeh (2012, pp. 19–20).) The overbar indicates an interior solution, i.e. the outer solutions far from the top and bottom boundary layers. The boundary layer functions $A(Z)$, $B(Z)$ and $C(Z)$ are the inner solutions that vanish at the boundaries $Z=0$ and approach unity in the interior where $Z \gg 1$.

3.4.1. *Interior solution*

Inserting (3.47)–(3.49) into (3.44)–(3.46) and setting $A=B=C=1$ yields

$$2\mu\, \bar{\psi}_{xx} + (2-\bar{\eta}_z)\, \bar{\xi}_x = 0, \tag{3.50}$$

$$\bar{\eta}_{zz} = 0, \tag{3.51}$$

$$\bar{\xi}_{xx} + (\bar{\eta}_z - 2)\bar{\psi}_x = 0. \tag{3.52}$$

Equation (3.51) implies that $\bar{\eta}$ is an affine function of z, which could also be inferred from (3.50) and (3.52) since $\bar{\psi}$ and $\bar{\xi}$ are functions of x only. The symmetry of the solution with respect to reflection about $z=0$ implies

$$\bar{\eta}(z) = \bar{\eta}_o\, z, \tag{3.53}$$

where $\bar{\eta}_o$ is to be determined.

Eliminating $\bar{\psi}$ between (3.50) and (3.52) gives

$$\bar{\xi}_{xxx} + \left(\frac{\bar{\eta}_o - 2}{\sqrt{2\mu}}\right)^2 \bar{\xi}_x = 0. \tag{3.54}$$

Periodicity with period 2Γ in x, together with $\xi_x(\pm\Gamma/2, z) = 0$, implies that

$$\bar{\xi} = \pm\bar{\xi}_o\, \sin(\pi x/\Gamma) \tag{3.55}$$

and

$$\bar{\eta}_o = 2 - \frac{\pi}{\Gamma}\sqrt{2\mu}, \tag{3.56}$$

where $\bar{\xi}_o > 0$ is another yet-to-be-determined constant. Another possible solution, $\bar{\eta}_o = 2 + (\pi/\Gamma)\sqrt{2\mu} > 2$, is discarded in light of the numerical results. Moreover, in § 3.4.3 it will be seen that $\bar{\eta}_o \leqslant 2$ because of the maximum principle, confirming that (3.56) is the only admissible solution.

Equation (3.52) then yields

$$\bar{\psi} = \frac{\pm\bar{\xi}_o}{\sqrt{2\mu}}\, \cos(\pi x/\Gamma), \tag{3.57}$$

so that the interior fields (i.e. the outer solutions) are known up to the one undetermined constant $\bar{\xi}_o$. (Notice that in (3.55) and (3.57), either $-\bar{\xi}_o$ or $+\bar{\xi}_o$ should be chosen for both $\bar{\psi}$ and $\bar{\xi}$.)

https://doi.org/10.1017/jfm.2014.306 Published online by Cambridge University Press

3.4.2. *Boundary layer solution*

The boundary conditions on the inner solutions are $A(0) = B(0) = C(0) = 0$ and $A(+\infty) = B(+\infty) = C(+\infty) = 1$. Focusing on the boundary layer adjacent to $z = +0.5$, (3.44)–(3.46) give, upon substitution of (3.47)–(3.49),

$$0 = 2\mu\,(\bar{\psi}_{xx}A + \bar{\psi}\,A''/\delta^2) + (2 - (\bar{\eta}_z\,C - \bar{\eta}\,C'/\delta))\,\bar{\xi}_x\,B, \tag{3.58}$$

$$0 = \bar{\eta}_{zz}\,C - 2\bar{\eta}_z\,C'/\delta + \bar{\eta}\,C''/\delta^2 - \bar{\psi}_x A\,\bar{\xi}\,B'/\delta + \bar{\xi}_x B\,\bar{\psi}\,A'/\delta, \tag{3.59}$$

$$0 = \bar{\xi}_{xx}B + \bar{\xi}\,B''/\delta^2 - (2 - (\bar{\eta}_z\,C - \bar{\eta}\,C'/\delta))\bar{\psi}_x A, \tag{3.60}$$

where a prime denotes $\mathrm{d}/\mathrm{d}Z$ (e.g. $A' \equiv \mathrm{d}A/\mathrm{d}Z$). Using the interior solutions (3.53) and (3.55)–(3.57) and observing that $\bar{\eta} \to \bar{\eta}_o/2$ as $z \to 0.5$, the above equations become

$$0 = \sqrt{2\mu}\left[-\left(\frac{\pi}{\Gamma}\right)^2 A + \frac{1}{\delta^2}A''\right] + \frac{\pi}{\Gamma}\left[2 - \left(2 - \frac{\pi}{\Gamma}\sqrt{2\mu}\right)\left(C - \frac{1}{2\delta}C'\right)\right]B, \tag{3.61}$$

$$0 = \left(2 - \frac{\pi}{\Gamma}\sqrt{2\mu}\right)\left[-\frac{2}{\delta}C' + \frac{1}{2\delta^2}C''\right] + \frac{\pi}{2\Gamma}\frac{\bar{\xi}_o^2}{\sqrt{2\mu}}\left[\frac{1}{\delta}AB' + \frac{1}{\delta}BA'\right], \tag{3.62}$$

$$0 = \sqrt{2\mu}\left[-\left(\frac{\pi}{\Gamma}\right)^2 B + \frac{1}{\delta^2}B''\right] + \frac{\pi}{\Gamma}\left[2 - \left(2 - \frac{\pi}{\Gamma}\sqrt{2\mu}\right)\left(C - \frac{1}{2\delta}C'\right)\right]A, \tag{3.63}$$

where (3.62) has been averaged over x to eliminate the $\sin^2(\pi x/\Gamma)$ and $\cos^2(\pi x/\Gamma)$ terms.

To balance the leading-order terms, we need to determine the boundary layer thickness δ as a function of a small parameter ϵ defined based on μ and Γ. We know that $\mu \ll 1$ to achieve the large-*Pe* limit, although from the above equations it seems that $\sqrt{\mu} \ll 1$ may be a more appropriate parameter in this problem. Here we restrict our analysis to $\Gamma \leqslant 1$, because the numerical results of § 3.3 showed that $\Gamma > 1$ does not maximize the transport.

With $\mu \ll 1$ and $\Gamma \leqslant 1$, we define the small parameter

$$\epsilon \equiv \frac{\Gamma\sqrt{2\mu}}{\pi} \tag{3.64}$$

(where the constants are included to simplify the algebra), and recognize that we must also consider the magnitude of

$$\sigma \equiv \Gamma/\sqrt{\mu}. \tag{3.65}$$

If $\Gamma = O(1)$, then $\sigma \gg 1$. The numerical results (figure 5) suggest that Γ_{opt} decreases as *Pe* increases. Therefore, we should also allow for the possibility that $\Gamma \ll 1$, implying $\sigma = O(1)$ or even $\sigma \ll 1$. Close examination of (3.61)–(3.63) reveals that $\sigma \gg 1$ and $\sigma = O(1)$ conveniently give the same balance and result in the same scaling for boundary layer thickness. Therefore, one solution covers both limits. Additionally, the distinguished limit $\sigma = O(1)$ guarantees that the solution is uniformly valid in Γ. Here we focus on these two limits. As demonstrated subsequently, the justification for excluding from our analysis the scenario in which $\sigma \ll 1$ is that Nu_{max} for a fixed value of Γ in the limit of large *Pe* is obtained with $\sigma \gg 1$, and that Nu_{MAX} for large *Pe* is achieved when $\sigma = O(1)$; see §§ 3.4.4 and 3.4.5.

https://doi.org/10.1017/jfm.2014.306 Published online by Cambridge University Press

Using definitions (3.64) and (3.65) in (3.61) and balancing the leading-order terms gives

$$A'' + \left(1 - \frac{\pi}{\sigma\sqrt{2}}\right) B\,C' = 0 \tag{3.66}$$

upon identifying

$$\delta = \epsilon. \tag{3.67}$$

Note that based on our restriction on σ, the term in parentheses is $O(1)$. The same procedure applied to (3.63) produces

$$B'' + \left(1 - \frac{\pi}{\sigma\sqrt{2}}\right) A\,C' = 0, \tag{3.68}$$

while (3.62) yields

$$\left(1 - \frac{\pi}{\sigma\sqrt{2}}\right) C'' + \frac{\bar{\xi}_o^2}{2}(AB' + BA') = 0. \tag{3.69}$$

Integrating equation (3.69), we see that

$$\left(1 - \frac{\pi}{\sigma\sqrt{2}}\right) C' = -\frac{\bar{\xi}_o^2}{2}(AB - 1), \tag{3.70}$$

where the constant of integration is determined by $C' \to 0$ and $A, B \to 1$ as $Z \to \infty$.

Substitution of (3.70) into (3.66) and (3.68) shows that A and B satisfy the same equation. Since they also satisfy the same boundary conditions, we conclude that $A = B$. In fact, making the ansatz $A = B = \rho C$ renders (3.69) identical to (3.66) and (3.68) upon setting the constant ρ equal to $(1 - \pi/(\sigma\sqrt{2}))/\bar{\xi}_o$. Making this ansatz, and again noting that C satisfies the same boundary conditions as do A and B (i.e. $A(+\infty) = B(+\infty) = C(+\infty) = 1$), we conclude that $A(Z) = B(Z) = C(Z)$ (i.e. $\rho = 1$). Therefore,

$$A'' + \bar{\xi}_o AA' = 0 \tag{3.71}$$

and

$$\bar{\xi}_o = 1 - \frac{\pi}{\sigma\sqrt{2}} \equiv 1 - \frac{\pi}{2\Gamma}\sqrt{2\mu} = \frac{\bar{\eta}_o}{2}. \tag{3.72}$$

Equation (3.71) can be integrated, giving

$$A' + \frac{\bar{\xi}_o}{2}A^2 = \frac{\bar{\xi}_o}{2}, \tag{3.73}$$

where again the constant of integration is determined from the boundary conditions $A' \to 0$ and $A \to 1$ as $Z \to \infty$. The exact solution is

$$A(Z) = \frac{1 - \exp(-\bar{\xi}_o Z)}{1 + \exp(-\bar{\xi}_o Z)} = \tanh\left[\frac{\bar{\xi}_o}{2}Z\right]. \tag{3.74}$$

https://doi.org/10.1017/jfm.2014.306 Published online by Cambridge University Press

3.4.3. *The complete solution: matching*

Upon including the bottom boundary layer and matching the three regions (the bulk and the two boundary layers), the complete asymptotic approximation is

$$\psi(x,z) \sim \frac{1}{\sqrt{2\mu}}\left(1-\frac{\pi}{2\Gamma}\sqrt{2\mu}\right)\cos\left(\frac{\pi}{\Gamma}x\right)H(z), \tag{3.75}$$

$$\xi(x,z) \sim \left(1-\frac{\pi}{2\Gamma}\sqrt{2\mu}\right)\sin\left(\frac{\pi}{\Gamma}x\right)H(z), \tag{3.76}$$

$$\eta(x,z) \sim 2\left(1-\frac{\pi}{2\Gamma}\sqrt{2\mu}\right)zH(z), \tag{3.77}$$

where

$$\begin{aligned} H(z) &= A\left(\frac{0.5-z}{\delta}\right)A\left(\frac{0.5+z}{\delta}\right) \\ &= \tanh\left[\frac{\pi}{2}\left(1-\frac{\pi}{2\Gamma}\sqrt{2\mu}\right)\frac{(0.5-z)}{\Gamma\sqrt{2\mu}}\right]\tanh\left[\frac{\pi}{2}\left(1-\frac{\pi}{2\Gamma}\sqrt{2\mu}\right)\frac{(0.5+z)}{\Gamma\sqrt{2\mu}}\right]. \end{aligned} \tag{3.78}$$

Therefore, to leading order, assuming that $\Gamma\sqrt{\mu}\ll 1$ and $\Gamma/\sqrt{\mu}$ is finite or large,

$$u(x,z) \sim \frac{1}{\sqrt{2\mu}}\left(1-\frac{\pi}{2\Gamma}\sqrt{2\mu}\right)\cos\left(\frac{\pi}{\Gamma}x\right)H'(z), \tag{3.79}$$

$$w(x,z) \sim \frac{1}{\sqrt{2\mu}}\left(\frac{\pi}{\Gamma}\right)\left(1-\frac{\pi}{2\Gamma}\sqrt{2\mu}\right)\sin\left(\frac{\pi}{\Gamma}x\right)H(z), \tag{3.80}$$

$$\theta(x,z) \sim \frac{1}{2}\left(1-\frac{\pi}{2\Gamma}\sqrt{2\mu}\right)\left(\sin\left(\frac{\pi}{\Gamma}x\right)+2z\right)H(z). \tag{3.81}$$

Many features of these asymptotic solutions are compared with the numerical results in Hassanzadeh (2012, figures 2.8 and 2.9) revealing excellent agreement for $Pe \geqslant O(1)$, uniformly over a wide range of Γ.

We note here that the maximum principle requires $|\theta| \leqslant 1$. Consequently, in (3.81), the first term in the parentheses, i.e. $\bar{\xi}_o = \bar{\eta}_o/2 = 1-(\pi/(2\Gamma))\sqrt{2\mu}$, has to be smaller than 1. This analysis justifies discarding the other solution for $\bar{\eta}_o$ in § 3.4.1.

Asymptotic approximations for Pe and Nu_{max} can be calculated analytically from (3.79)–(3.81):

$$Pe \equiv \sqrt{\langle u^2+w^2\rangle} = \frac{1}{2\sqrt{\mu}}\left(1-\frac{\pi}{2\Gamma}\sqrt{2\mu}\right)\sqrt{\int_{-0.5}^{0.5}\left\{(H')^2+(\pi/\Gamma)^2H^2\right\}\mathrm{d}z}, \tag{3.82}$$

$$Nu_{max} \equiv 1+\langle w\theta\rangle = 1+\frac{1}{4\sqrt{2\mu}}\left(\frac{\pi}{\Gamma}\right)\left(1-\frac{\pi}{2\Gamma}\sqrt{2\mu}\right)^2\int_{-0.5}^{0.5}H^2\,\mathrm{d}z. \tag{3.83}$$

Because $H(z)$ depends on μ and Γ, it is difficult to find an explicit expression for $Nu_{max}(Pe,\Gamma)$. However, (3.82) and (3.83) can easily be evaluated numerically for a given pair of (μ,Γ). Figure 7 compares the values of $Nu_{max}(Pe,\Gamma)$ from the numerical solutions with the values given by (3.82) and (3.83) for $\Gamma=0.2$ and 1. The numerical and analytical results agree well, even for relatively small values of

https://doi.org/10.1017/jfm.2014.306 Published online by Cambridge University Press

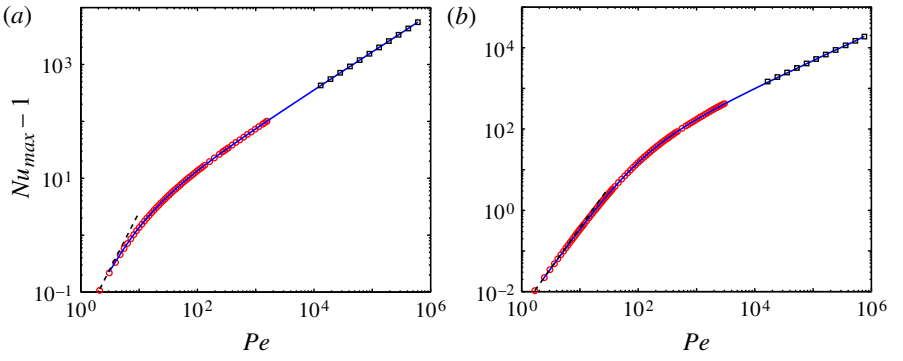


FIGURE 7. (Colour online) Plots of Nu_{max} from the numerical solutions (red circles), the small-Pe analytical solution (3.31) (black dashed lines) and the large-Pe asymptotic solution (3.82) and (3.83) (blue solid lines) for two cases: (*a*) $\Gamma = 1$; (*b*) $\Gamma = 0.2$. The black squares show (3.88).

Pe, suggesting that the higher-order terms may be transcendentally small in ϵ. (The numerically inspired ansatzen $\psi = a(z)\cos(\pi x/\Gamma)$, $\xi = b(z)\sin(\pi x/\Gamma)$ and $\eta = c(z)$ separate (3.44)–(3.46) into ordinary differential equations for $a(z)$, $b(z)$ and $c(z)$ without approximation. The exact solutions of those ordinary differential equations involve elliptic functions which are well known to be exponentially accurately approximated by products of tanh functions.)

3.4.4. $Nu_{max}(Pe, \Gamma)$*: the* $\epsilon \ll 1$ *and* $\sigma \gg 1$ *limit*

In the limit of relatively small $\epsilon \equiv \Gamma\sqrt{2\mu}/\pi$, the integrals in (3.82) and (3.83) are approximately

$$\int_{-0.5}^{0.5} H^2 \,\mathrm{d}z \;\approx\; 1 - \left[\frac{4\epsilon}{1 - \pi/(\sigma\sqrt{2})}\right], \tag{3.84}$$

$$\int_{-0.5}^{0.5} (H')^2 \,\mathrm{d}z \;\approx\; \frac{2}{3}\left[\frac{1 - \pi/(\sigma\sqrt{2})}{\epsilon}\right], \tag{3.85}$$

as has been confirmed numerically (again, recall that $\sigma \equiv \Gamma/\sqrt{\mu}$ is not small compared to 1). Consider (3.82) and (3.83) in the limit of vanishing μ and fixed Γ, i.e. $\epsilon \ll 1$ and $\sigma \gg 1$. In this limit, (3.84) and (3.85) further simplify to 1 and $2/(3\epsilon)$, respectively. Then (3.82) and (3.83) yield

$$Pe \;=\; \frac{1}{\sqrt{2}\epsilon}\sqrt{\frac{\sqrt{2}}{3\pi}\sigma}, \tag{3.86}$$

$$Nu_{max} \;=\; 1 + \frac{1}{4\epsilon}. \tag{3.87}$$

Solving (3.86) for μ and substituting into (3.87) yields $Nu_{max}(Pe, \Gamma)$ as

$$Nu_{max} = 1 + \frac{1}{4}\left[\frac{3\pi^2}{\Gamma^2}\right]^{1/3} Pe^{2/3}. \tag{3.88}$$

The accuracy of this approximation is demonstrated in figure 7 for $\Gamma = 0.2$ and 1.

https://doi.org/10.1017/jfm.2014.306 Published online by Cambridge University Press

Equation (3.88) gives Nu_{max} as a function of Pe for a fixed value of Γ, which is not the same as Nu_{MAX}, i.e. the maximum achievable Nu_{max} at that Pe. Determining $Nu_{MAX}(Pe)$ requires letting Γ shrink as Pe increases, which is analysed next.

3.4.5. *$Nu_{MAX}(Pe)$: the $\epsilon \ll 1$ and $\sigma = O(1)$ limit*

Here we examine the limit $\sqrt{\mu} \ll 1$ and $\Gamma \ll 1$ when their ratio is finite. Physically this means that we allow the cells to narrow as Pe increases. It is in this distinguished limit that Nu_{MAX} for a given Pe, i.e. the optimal transport for a given amount of energy, is achieved.

In this limit, (3.84) again reduces to 1, but (3.85) cannot be further simplified. Using these approximations for the integrals in (3.82) and (3.83) implies that

$$Pe = \frac{1}{\sqrt{2}\epsilon}\left(1 - \frac{\pi}{\sigma\sqrt{2}}\right)\sqrt{\frac{2}{3} + \frac{\sqrt{2}}{3\pi}\sigma}, \tag{3.89}$$

$$Nu_{max} - 1 = \frac{1}{4\epsilon}\left(1 - \frac{\pi}{\sigma\sqrt{2}}\right)^2. \tag{3.90}$$

Dividing (3.90) by (3.89) to eliminate ϵ yields

$$\frac{Nu_{max} - 1}{Pe} = \frac{1}{2\sqrt{2}} \frac{\left(1 - \dfrac{\pi}{\sigma\sqrt{2}}\right)}{\sqrt{\dfrac{2}{3} + \dfrac{\sqrt{2}}{3\pi}\sigma}}, \tag{3.91}$$

which is maximized at

$$\sigma_{opt} \equiv \frac{\Gamma_{opt}}{\sqrt{\mu}} = 2\sqrt{2}\pi \approx 8.885\,766. \tag{3.92}$$

This calculation thus gives the optimal aspect ratio Γ_{opt} that maximizes Nu_{max} at a given μ. Using $\sigma = \sigma_{opt}$ in (3.91) gives $Nu_{MAX}(Pe)$ as

$$Nu_{MAX} = 1 + 0.1875\,Pe. \tag{3.93}$$

Figure 5 shows that (3.93) gives the maximum possible transport with remarkable accuracy. Finally, combining (3.89) and (3.92) determines $\Gamma_{opt}(Pe)$, the optimal cell aspect ratio at a given Pe:

$$\Gamma_{opt} = 3.8476\,Pe^{-1/2}. \tag{3.94}$$

Thinner cells produce the maximum transport as the Péclet number increases.

3.5. *Example: application to porous media convection*

We now show how Rayleigh–Bénard convection in a fluid-saturated porous layer is an example of transport with fixed energy, in order to express Nu_{max} and Nu_{MAX} as functions of the Rayleigh number Ra and to compare the optimal transport bounds with the results of previous analytical and numerical investigations.

Rayleigh–Bénard convection in a fluid-saturated porous layer heated from below and cooled from above is often modelled by the system

https://doi.org/10.1017/jfm.2014.306 Published online by Cambridge University Press

$$\boldsymbol{\nabla}\cdot\boldsymbol{v} \;=\; 0, \tag{3.95}$$

$$\frac{1}{Pr}\left(\dot{\boldsymbol{v}}+\boldsymbol{v}\cdot\boldsymbol{\nabla}\boldsymbol{v}\right)+\boldsymbol{v} \;=\; -\boldsymbol{\nabla}p+Ra\,T\hat{\boldsymbol{z}}, \tag{3.96}$$

$$\dot{T}+\boldsymbol{v}\cdot\boldsymbol{\nabla}T \;=\; \Delta T, \tag{3.97}$$

with the same boundary conditions as used in the preceding sections: $T|_{z=0}=1$, $T|_{z=1}=0$ and $\hat{\boldsymbol{z}}\cdot\boldsymbol{v}|_{z=0}=\hat{\boldsymbol{z}}\cdot\boldsymbol{v}|_{z=1}=0$. In this system Pr is the Prandtl–Darcy number and Ra is the Rayleigh number (see, e.g., Doering & Constantin 1998 and references therein for more details).

Taking the inner product of (3.96) with $\boldsymbol{v}$ and averaging over long times and over the spatial domain with impermeable walls yields

$$\left\langle|\boldsymbol{v}|^2\right\rangle = Ra\,\langle wT\rangle\,. \tag{3.98}$$

The transient term vanishes owing to the long-time averaging (when the kinetic energy is $o(t)$ as $t\to\infty$), and the nonlinear and pressure terms vanish because of the spatial integration. Then, using the definition of Pe in (2.13) for fixed energy problems, and with Nu given by (2.15) from § 2, we identify

$$Pe^2 = Ra\,(Nu-1). \tag{3.99}$$

The Nusselt number Nu, when calculated by long-time averaging, is solely a function of Ra and the domain aspect ratio Γ (and possibly initial data). Consequently, in steady and statistically steady flows, (3.99) shows that the time-averaged Péclet number is fixed for given values of Γ and Ra (and possibly initial data); note that Ra depends on the fluid properties and the imposed temperature difference between the walls, not on the flow. Therefore, steady convection in porous media occurs with 'fixed' energy.

Employing (3.99), Pe can be replaced with Ra in (3.88), (3.93) and (3.94) so that

$$Nu_{max}(Ra,\,\Gamma) \;=\; 1+\frac{\sqrt{3}\pi}{8\Gamma}\,Ra^{1/2}, \tag{3.100}$$

$$Nu_{MAX}(Ra) \;=\; 1+0.0352\,Ra, \tag{3.101}$$

$$\Gamma_{opt} \;=\; 8.89\,Ra^{-1/2}. \tag{3.102}$$

Interestingly, $\Gamma\sim Ra^{-1/2}$ is the scaling of the shortest-wavelength unstable mode about the conduction solution in porous media convection.

Table 1 compares the optimal (steady) transport derived here with pertinent results obtained using other methods. The classical argument of Malkus (1954) and Howard (1964) based on the marginal stability of the boundary layer predicts $Nu\sim Ra$ for Rayleigh–Bénard convection in a fluid-saturated porous layer (Horne & O'Sullivan 1978). The background method – which, we note, does not enforce the full advection–diffusion equation for the temperature – also implies an upper bound on Nu that scales linearly with Ra. The prefactors in the upper bound have been improved over the years (Doering & Constantin 1998; Otero *et al.* 2004; Wen *et al.* 2012).

We emphasize that in this work, (3.95) and the steady version of (3.97) were solved for one cell, but the momentum equation (3.96) was not imposed. Related analysis of steady cellular flows of the full Rayleigh–Bénard system was done recently by Corson (2011), who used numerical continuation in a single convection cell to solve the steady version of (3.95)–(3.97) in the limit of infinite Prandtl–Darcy number,

https://doi.org/10.1017/jfm.2014.306 Published online by Cambridge University Press

	$Nu(Ra)$	$\Gamma(Ra)$	$Nu(Ra, \Gamma_{fixed})$
Boundary layer stability argument			
Malkus (1954), Howard (1964) and Horne & O'Sullivan (1978)	$\sim C\,Ra$		
Background method (upper bounds)			
Doering & Constantin (1998)	$\leqslant 0.035\,Ra$		
Otero *et al.* (2004)	$\leqslant 0.029\,Ra$		
Wen *et al.* (2012)	$\lesssim 0.017\,Ra$		
Unsteady simulations (DNS)			
Otero *et al.* (2004): $Ra \leqslant 10^4$	$\sim C\,Ra^{0.9}$		
Hewitt, Neufeld & Lister (2012): $Ra \leqslant 4 \times 10^4$	$\sim 0.007\,Ra$	$\sim C\,Ra^{-0.4}$	
Steady unicellular analysis			
Fowler (1997)			$\sim C(\Gamma)\,Ra^{1/3}$
Corson (2011)	$\sim C\,Ra^{2/3}$	$\sim C\,Ra^{-1/2}$	$\sim C(\Gamma)\,Ra^{1/3}$
Current work			
Numerical and asymptotic analyses	$\leqslant 1 + 0.035\,Ra$	$\sim 8.89\,Ra^{-1/2}$	$\leqslant 1 + (0.68/\Gamma)\,Ra^{1/2}$

TABLE 1. Comparison of the results of the current work with the scalings for porous media convection obtained using various other methods.

finding that $Nu \sim Ra^{2/3}$ and $\Gamma \sim Ra^{-1/2}$. Furthermore, Corson (2011) showed that Nu scales as $Ra^{1/3}$ for steady convection when the cell size Γ is fixed. Comparison of these scalings with those obtained in the current work shows that steady convection in porous media does not transport as much heat as is possible by a steady flow with the same energy.

On the other hand, the latest two-dimensional direct numerical simulations (DNS) of Rayleigh–Bénard convection in a porous layer with infinite Prandtl–Darcy number, for Ra as high as 4×10^4, show that $Nu \sim Ra$ for 'turbulent' flows and that the emergent cells that form in the bulk have an aspect ratio that scales approximately as $Ra^{-0.4}$ (Hewitt *et al.* 2012). Comparing the steady (Corson 2011) and unsteady (Hewitt *et al.* 2012) solutions of (3.95)–(3.97), it is evident that unsteadiness enhances the transport. The maximum possible steady transport scales linearly with Ra, which, perhaps curiously, coincides with the unsteady results. However, the unsteady transport is around five times smaller than the maximum possible steady transport at a given Ra (current work), and the convection cells of the unsteady flow are wider than the optimal cells with aspect ratio Γ_{opt} (see table 1). A recent investigation, for example, suggests that cells with aspect ratio smaller than Γ, where $\Gamma \sim Ra^{-5/14}$, are dynamically unstable at high Ra (Hewitt, Neufeld & Lister 2013), which might explain the wider cells and (slightly) less-than-optimal transport observed in the DNS of unsteady flows.

4. Optimal transport with fixed enstrophy

In the second version of the optimal transport problem, we investigate steady flows with fixed enstrophy. Then (2.8)–(2.11) and (2.14) become

$$\boldsymbol{v} \cdot \boldsymbol{\nabla}\theta = \Delta\theta + w, \tag{4.1}$$

https://doi.org/10.1017/jfm.2014.306 Published online by Cambridge University Press

$$\boldsymbol{\nabla}\cdot\boldsymbol{v}=0, \tag{4.2}$$

$$Pe^2=\left\langle|\boldsymbol{\nabla}\boldsymbol{v}|^2\right\rangle, \tag{4.3}$$

$$\theta(x,0)=\theta(x,1)=0, \tag{4.4}$$

$$w(x,0)=w(x,1)=0. \tag{4.5}$$

Exactly as for the fixed energy problem, simple analysis gives an *a priori* upper bound on Nu. Starting from (2.15),

$$\begin{aligned} Nu &= 1+\langle wT\rangle = 1+\langle w(T-1/2)\rangle \\ &\leqslant 1+\left\langle w^2\right\rangle^{1/2}\left\langle (T-1/2)^2\right\rangle^{1/2} \\ &\leqslant 1+\frac{\left\langle|\boldsymbol{\nabla}w|^2\right\rangle^{1/2}}{2\pi}\leqslant 1+\frac{\left\langle|\boldsymbol{\nabla}\boldsymbol{v}|^2\right\rangle^{1/2}}{2\pi} \\ &= 1+\frac{Pe}{2\pi} \end{aligned} \tag{4.6}$$

where, as before, incompressibility and the Cauchy–Schwarz inequality were used in the first two lines. The maximum principle for the temperature and the Poincaré's inequality ($\langle(\partial w/\partial z)^2\rangle\geqslant\pi^2\langle w^2\rangle$) were then applied to derive the first term on the third line and (4.3) was used to obtain the final result. As will be seen, this upper bound is much too high for this problem.

4.1. *Variational formulation for steady flows*

The variational formulation of the fixed enstrophy problem involves maximizing Nu with constraints (4.1)–(4.3) and boundary conditions (4.4) and (4.5). The relevant functional is

$$\mathcal{F}=\left\langle w\theta-\phi(x,z)\,(\boldsymbol{v}\cdot\boldsymbol{\nabla}\theta-\Delta\theta-w)+p(x,z)\,(\boldsymbol{\nabla}\cdot\boldsymbol{v})+\frac{\mu}{2}\left(|\boldsymbol{\nabla}\boldsymbol{v}|^2-Pe^2\right)\right\rangle, \tag{4.7}$$

where $\phi(x,z)$, $p(x,z)$ and μ are again Lagrange multipliers. The Euler–Lagrange equations are

$$\boldsymbol{0}=\frac{\delta\mathcal{F}}{\delta\boldsymbol{v}}=(\theta+\phi)\,\hat{\boldsymbol{z}}+\theta\,\boldsymbol{\nabla}\phi-\boldsymbol{\nabla}p+\mu\Delta\boldsymbol{v}, \tag{4.8}$$

$$0=\frac{\delta\mathcal{F}}{\delta\theta}=\boldsymbol{v}\cdot\boldsymbol{\nabla}\phi+\Delta\phi+w, \tag{4.9}$$

$$0=\frac{\delta\mathcal{F}}{\delta\phi}=-\boldsymbol{v}\cdot\boldsymbol{\nabla}\theta+\Delta\theta+w, \tag{4.10}$$

$$0=\frac{\delta\mathcal{F}}{\delta p}=\boldsymbol{\nabla}\cdot\boldsymbol{v}, \tag{4.11}$$

$$0=\frac{\partial\mathcal{F}}{\partial\mu}=\frac{1}{2}\left(\left\langle|\boldsymbol{\nabla}\boldsymbol{v}|^2\right\rangle-Pe^2\right), \tag{4.12}$$

where ϕ vanishes at $z=0$ and $z=1$. To eliminate the surface term coming from $\boldsymbol{\nabla}\cdot(\boldsymbol{v}\boldsymbol{\nabla}\boldsymbol{v})$, we can use either the stress-free ($\partial u/\partial z=0$) or the no-slip ($u=0$) boundary condition at $z=0$ and $z=1$. Therefore, the full set of boundary conditions is

$$w(x,0)\;=\;w(x,1)=0, \tag{4.13}$$

https://doi.org/10.1017/jfm.2014.306 Published online by Cambridge University Press

$$\theta(x,0) = \theta(x,1) = 0, \tag{4.14}$$

$$\phi(x,0) = \phi(x,1) = 0, \tag{4.15}$$

together with either

$$u(x,0) = u(x,1) = 0 \quad \text{(no-slip)} \tag{4.16}$$

or

$$\left.\frac{\partial u}{\partial z}\right|_{z=0} = \left.\frac{\partial u}{\partial z}\right|_{z=1} = 0 \quad \text{(stress-free)}. \tag{4.17}$$

In the following, we restrict attention to the stress-free boundary condition (4.17), leaving the no-slip problem for future work.

4.2. *The limit of small Pe: asymptotic solution*

In the limit of small *Pe*, when $|\boldsymbol{v}| \ll 1$ we can linearize the Euler–Lagrange equations as follows:

$$-\mu\,\Delta\boldsymbol{v} + \boldsymbol{\nabla} p = (\theta+\phi)\hat{\boldsymbol{z}}, \tag{4.18}$$

$$\Delta\phi + w = 0, \tag{4.19}$$

$$\Delta\theta + w = 0, \tag{4.20}$$

$$\boldsymbol{\nabla}\cdot\boldsymbol{v} = 0. \tag{4.21}$$

Subtracting (4.20) from (4.19) and using (4.14) and (4.15) establishes that $\theta = \phi$ in the small-*Pe* regime. Then, eliminating p from (4.18) results in

$$-\mu\Delta\Delta w = \theta_{xx} + \phi_{xx} = 2\,\theta_{xx}, \tag{4.22}$$

which, along with (4.20) and (4.21) and the boundary conditions (4.13), (4.14) and (4.17), can be solved analytically to find $(\boldsymbol{v}, \theta)$ in this small-*Pe* limit. Following the same procedure and notation as used in § 3.2 (see appendix B), we obtain

$$Nu = 1 + \frac{k^2}{(m^2\pi^2 + k^2)^3}\,Pe^2, \tag{4.23}$$

which, for given values of *Pe* and $\Gamma = \pi/k$, is maximized at $m = 1$. As a result, using the notation defined in § 2.1, we have

$$Nu_{max}(Pe, \Gamma) = 1 + \frac{\Gamma^4}{\pi^4(\Gamma^2+1)^3}\,Pe^2. \tag{4.24}$$

The largest value of $Nu_{max}(Pe, \Gamma)$ is achieved at $\Gamma_{opt} = \sqrt{2}$, so

$$Nu_{MAX}(Pe) = 1 + \frac{Pe^2}{(27\pi^4/4)}. \tag{4.25}$$

Maximum transport in the limit of small *Pe* is achieved by an array of cells with aspect ratio $\Gamma_{opt} = \sqrt{2}$ (see Hassanzadeh 2012, figure 3.1). This flow resembles Rayleigh–Bénard convection in a pure fluid layer (with stress-free boundary conditions) at the onset of linear instability (Drazin & Reid 2004). The factor $27\pi^4/4$ in (4.25) is, in fact, precisely the critical *Ra* of the instability.

https://doi.org/10.1017/jfm.2014.306 Published online by Cambridge University Press

4.3. *Small to large Pe: numerical solution*

Following the same steps as in the fixed energy case and using $\omega = \Delta\psi$, (4.8)–(4.11) simplify to

$$\mathrm{J}(\theta, \phi) - \mu\,\Delta\omega + (\theta + \phi)_x = 0, \tag{4.26}$$

$$\Delta\psi - \omega = 0, \tag{4.27}$$

$$-\mathrm{J}(\psi, \theta) - \Delta\theta + \psi_x = 0, \tag{4.28}$$

$$-\mathrm{J}(\psi, \phi) + \Delta\phi - \psi_x = 0, \tag{4.29}$$

and the boundary conditions (4.13)–(4.15) and (4.17) become

$$\psi(x, 0) = \psi(x, 1) = 0, \tag{4.30}$$

$$\omega(x, 0) = \omega(x, 1) = 0, \tag{4.31}$$

$$\theta(x, 0) = \theta(x, 1) = 0, \tag{4.32}$$

$$\phi(x, 0) = \phi(x, 1) = 0, \tag{4.33}$$

where ω has been introduced to avoid the occurrence of fourth-order derivatives and to simplify the implementation of boundary conditions.

Using the same continuation algorithm as given in § 3.3.1, and following the steps described in § 3.3.2 and appendix A, (4.26)–(4.29) become

$$\begin{bmatrix} \mu\Delta & -\boldsymbol{I} & \boldsymbol{O} & \boldsymbol{O} \\ \boldsymbol{O} & \mu\Delta & -(\boldsymbol{I} + \boldsymbol{\phi}_z^N)\boldsymbol{D}_x + \boldsymbol{\phi}_x^N\boldsymbol{D}_z & -(\boldsymbol{I} - \boldsymbol{\theta}_z^N)\boldsymbol{D}_x - \boldsymbol{\theta}_x^N\boldsymbol{D}_z \\ -(\boldsymbol{I} - \boldsymbol{\theta}_z^N)\boldsymbol{D}_x - \boldsymbol{\theta}_x^N\boldsymbol{D}_z & \boldsymbol{O} & \Delta - \boldsymbol{\psi}_z^N\boldsymbol{D}_x + \boldsymbol{\psi}_x^N\boldsymbol{D}_z & \boldsymbol{O} \\ -(\boldsymbol{I} + \boldsymbol{\phi}_z^N)\boldsymbol{D}_x + \boldsymbol{\phi}_x^N\boldsymbol{D}_z & \boldsymbol{O} & \boldsymbol{O} & \Delta + \boldsymbol{\psi}_z^N\boldsymbol{D}_x - \boldsymbol{\psi}_x^N\boldsymbol{D}_z \end{bmatrix} \begin{bmatrix} \delta\boldsymbol{\psi} \\ \delta\boldsymbol{\omega} \\ \delta\boldsymbol{\theta} \\ \delta\boldsymbol{\phi} \end{bmatrix}$$

$$= \begin{bmatrix} -\Delta\boldsymbol{\psi}^N + \boldsymbol{\omega}^N \\ -\mu\Delta\boldsymbol{\omega}^N + (\boldsymbol{I} + \boldsymbol{\phi}_z^N)\boldsymbol{\theta}_x^N + (\boldsymbol{I} - \boldsymbol{\theta}_z^N)\boldsymbol{\phi}_x^N \\ -\Delta\boldsymbol{\theta}^N + (\boldsymbol{I} - \boldsymbol{\theta}_z^N)\boldsymbol{\psi}_x^N + \boldsymbol{\psi}_z^N\boldsymbol{\theta}_x^N \\ -\Delta\boldsymbol{\phi}^N + (\boldsymbol{I} + \boldsymbol{\phi}_z^N)\boldsymbol{\psi}_x^N - \boldsymbol{\psi}_z^N\boldsymbol{\phi}_x^N \end{bmatrix}. \tag{4.34}$$

The details of the matrix algebra and boundary condition implementation are the same as before (see § 3.3.2). The results presented here were obtained using $M = 61$ or 81. As before, the iterative solution always converged in fewer than six iterations.

4.3.1. *Numerical results*

Figure 8 shows ψ and θ for the case where $\Gamma = \sqrt{2}/\pi^3$ for low to high values of Pe. The value of Nu_{max} increases with Pe, and the flow structure changes. The enhancement of the heat transport is associated with the development of the boundary layers: the boundary layers thin as Pe increases and result in larger Nu_{max}. However, in contrast to the fixed energy problem, a (re)circulation zone emerges between the boundary layers and the bulk at large values of Pe.

The high-Pe circulation zone complicates the flow structure for ξ and η as well. Figure 9 shows $(\psi, \theta, \phi, \xi, \eta)$ for $\Gamma = \sqrt{2}/\pi^2$ in the limit of large Pe. (The small-scale wiggles in the level sets are due in part to insufficient plotting resolution.) The optimal flow field for the fixed enstrophy problem is thus more complicated than the optimal flow field for the fixed energy problem, mainly due to the presence of the circulation zone. Nevertheless, the bulk flows in the two problems are similar: ψ and ξ are nearly

https://doi.org/10.1017/jfm.2014.306 Published online by Cambridge University Press

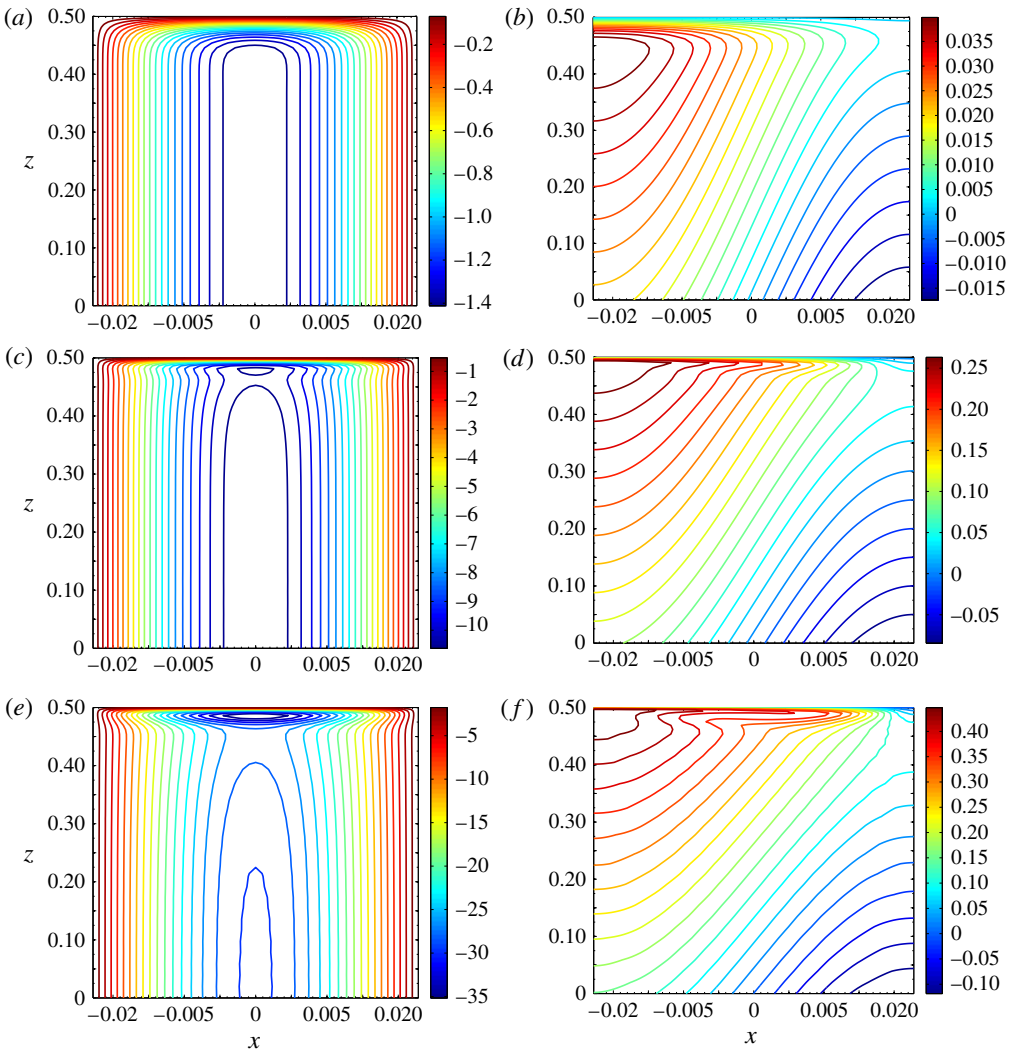


FIGURE 8. (Colour online) Evolution of the flow field with increasing Pe for the case where $\Gamma = \sqrt{2}/\pi^3$. (*a*,*c*,*e*) show ψ and (*b*,*d*,*f*) show θ; only the upper half of the domain is shown for better illustration of the circulation zone. (*a*,*b*) $Pe = 4889.1$, $Nu_{max} = 1.98$; (*c*,*d*) $Pe = 3.97 \times 10^4$, $Nu_{max} = 40.1$; (*e*,*f*) $Pe = 1.43 \times 10^5$, $Nu_{max} = 175.6$. The resolution is 81^2.

independent of z and have a single-mode dependence on x; η appears to be linear in z, as before, and nearly x-independent. Appendix C presents the interior solution for this problem:

$$\bar{\xi} = \pm\bar{\xi}_o \sin(\pi x/\Gamma), \tag{4.35}$$

$$\bar{\eta}_o = 2 - \left(\frac{\pi}{\Gamma}\right)^2 \sqrt{2\mu}, \tag{4.36}$$

$$\bar{\psi} = \frac{\pm\bar{\xi}_o}{(\pi/\Gamma)\sqrt{2\mu}} \cos(\pi x/\Gamma), \tag{4.37}$$

https://doi.org/10.1017/jfm.2014.306 Published online by Cambridge University Press

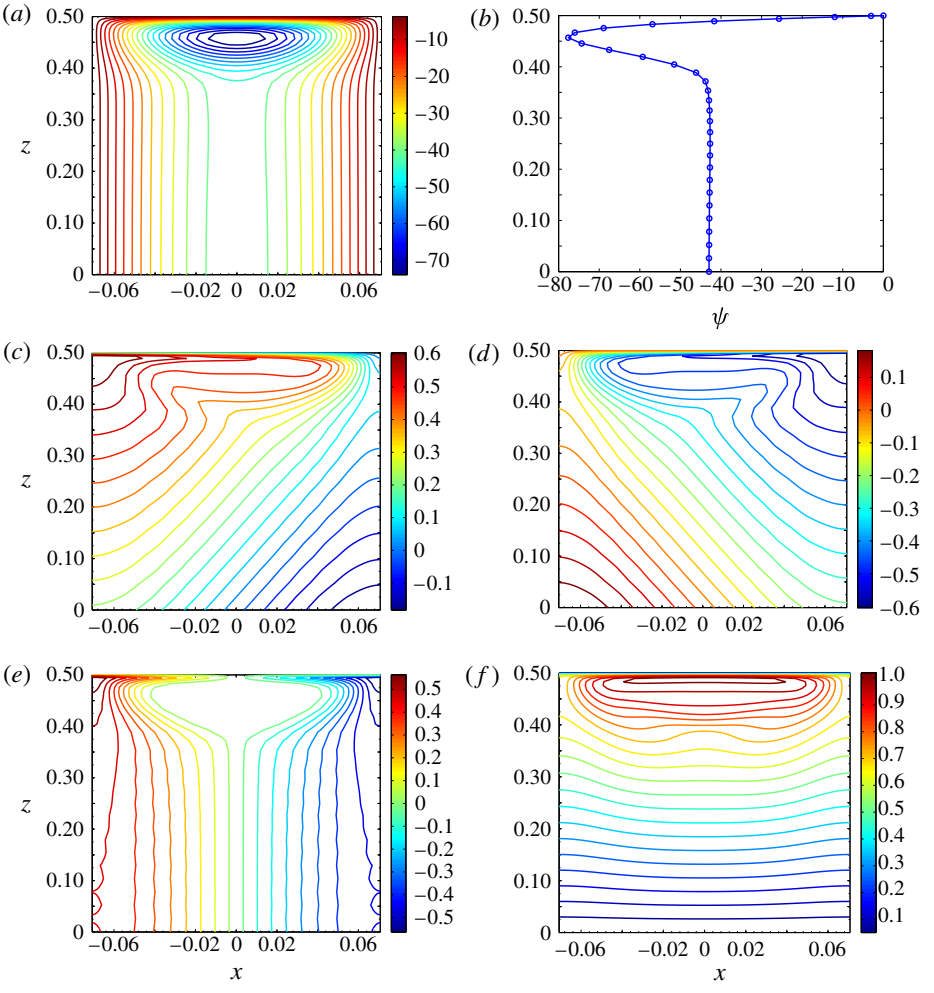


FIGURE 9. (Colour online) Flow field for $\Gamma = \sqrt{2}/\pi^2$, $\mu = 4.83 \times 10^{-8}$, $Pe = 3.57 \times 10^4$ and $Nu_{max} = 103.3.7$; only the upper half of the domain is shown for better illustration of the circulation zone. (*a*) ψ; (*b*) ψ along $x = 0$; (*c*) θ; (*d*) ϕ; (*e*) $\xi \equiv \theta + \phi$; (*f*) $\eta \equiv \theta - \phi$. The resolution is 61^2.

which agrees with the numerical results. This solution is determined up to an unknown constant $\bar{\xi}_o$ that should be determinable from the boundary layer solution, but owing to the complexity of this flow we have not yet succeeded in solving the boundary layer equations to complete the required matched asymptotic analysis.

In the absence of an analytical solution, we use the numerical results to find $Nu_{max}(Pe,\ \Gamma)$ and $Nu_{MAX}(Pe)$. Figure 10 is a plot of the numerically calculated $Nu_{max}(Pe,\ \Gamma)$ for several values of Γ. Several conclusions drawn from the results presented in figure 5 also hold for the fixed enstrophy problem: Nu_{max} agrees with (4.24) in the limit of small Pe (benchmarking the code), and the absolute upper bound (4.6) quantitatively overestimates transport, albeit in the Péclet-number scaling in this case. For fixed Γ and large Pe, we observe that

$$Nu_{max}(Pe,\ \Gamma) = 1 + K(\Gamma)\, Pe^{1/2}, \tag{4.38}$$

https://doi.org/10.1017/jfm.2014.306 Published online by Cambridge University Press

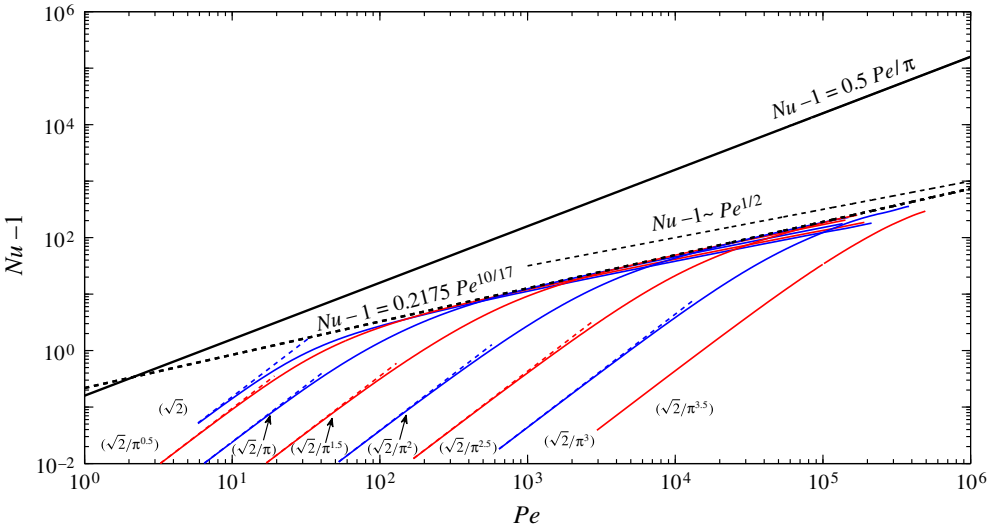


FIGURE 10. (Colour online) The numerically obtained Nu_{max} as a function of Pe for various values of Γ (blue and red lines). The labels in parentheses show Γ. For each case, the short dashed line of the same colour, visible in most cases, shows the analytical Nu_{max}, (4.24), in the small-Pe limit. The thick black solid line shows the absolute upper bound (4.6), and the thick black dashed line shows a fit to the envelope (i.e. Nu_{MAX}; see (4.39)). The thin black dashed line indicates the $Pe^{1/2}$ slope. All numerical results were obtained by continuing the linear solutions with $m = 1$, and all results shown here have resolution $M = 61$. Using a higher resolution $M = 81$ results in negligible changes to the plot.

where $K(\Gamma)$ is a prefactor that can be determined from the numerical results. A fit to the envelope made by the largest values of Nu_{max} gives

$$Nu_{MAX}(Pe) = 1 + 0.2175\, Pe^{0.58}. \tag{4.39}$$

For reasons that will become clear immediately below in the next subsection, we conjecture that the measured exponent 0.58 in (4.39) is really $10/17 = 0.5882\ldots$ for large values of Pe.

More data points in Γ, especially for smaller Γ, are needed to determine $\Gamma_{opt}(Pe)$ accurately from the numerical results. Using just three points in the wide range of Pe from 1701 to 4.1×10^4, however, we obtain estimates -0.361 and -0.358 for the exponent of Pe in the scaling of $\Gamma_{opt}(Pe)$. For the same reasons alluded to above (which will become clear below), we conjecture that this exponent is really $6/17 = 0.3529\ldots$ for large Pe.

4.4. *Example: application to Rayleigh–Bénard convection*

Classical Rayleigh–Bénard convection in a layer of pure fluid heated from below and cooled from above is, at least in the (statistically) steady case, an example of transport with fixed enstrophy. Rayleigh (1916) modelled this problem with the Boussinesq equations

$$\boldsymbol{\nabla} \cdot \boldsymbol{v} = 0, \tag{4.40}$$

https://doi.org/10.1017/jfm.2014.306 Published online by Cambridge University Press

$$\frac{1}{Pr}\left(\dot{\boldsymbol{v}} + \boldsymbol{v}\cdot\boldsymbol{\nabla}\boldsymbol{v}\right) = -\boldsymbol{\nabla}p + \Delta\boldsymbol{v} + Ra\,T\hat{\boldsymbol{z}}, \tag{4.41}$$

$$\dot{T} + \boldsymbol{v}\cdot\boldsymbol{\nabla}T = \Delta T, \tag{4.42}$$

where Pr is the Prandtl number. Taking the inner product of (4.41) with $\boldsymbol{v}$ and integrating over long time and over a domain with impermeable walls yields

$$0 = -\left\langle |\boldsymbol{\nabla}\boldsymbol{v}|^2 \right\rangle + Ra\,\langle wT\rangle\,. \tag{4.43}$$

Using the definition (2.14) of Pe for fixed enstrophy problems and the definition (2.15) of Nu from § 2, we obtain

$$Pe^2 = Ra\,(Nu - 1). \tag{4.44}$$

The Nusselt number Nu is a function of Ra and the aspect ratio Γ, and as a result Pe is fixed for given values of these parameters. (As before, the control parameter Ra depends on the fluid properties and the imposed temperature difference between the walls, but not on the flow.) Hence, (statistically) steady Rayleigh–Bénard convection in a pure fluid layer occurs with fixed enstrophy.

Employing (4.44) to replace Pe with Ra in (4.38) and (4.39), the bounds are

$$Nu_{max}(Ra,\,\Gamma) = 1 + (K(\Gamma))^{4/3}\,Ra^{1/3}, \tag{4.45}$$

$$Nu_{MAX}(Ra) = 1 + 0.1152\,Ra^{5/12}. \tag{4.46}$$

Furthermore, using the rather crude estimates for the exponent of Pe in $\Gamma_{opt}(Pe)$ gives

$$\Gamma_{opt}(Ra) \sim Ra^{-0.2546}. \tag{4.47}$$

Interestingly, $\Gamma \sim k^{-1} \sim Ra^{-0.25}$ is the scaling of the shortest-wavelength unstable mode for Rayleigh–Bénard convection in pure fluids with stress-free boundaries, which corresponds to the conjecture that $\Gamma_{opt}(Pe) \sim Pe^{-6/17}$.

Table 2 compares the bounds discovered here with the results of other analyses of Rayleigh–Bénard convection. The classical marginally stable boundary layer argument of Malkus (1954) and Howard (1964) predicts that $Nu \sim Ra^{1/3}$ uniformly in the Prandtl number. On the other hand, the argument of Spiegel (1962) based on the assumption that transport is limited by the ballistic motions across the bulk (see also Kraichnan 1962) suggests that $Nu \sim (Pr\,Ra)^{1/2}$. While both of these arguments are independent of the spatial dimension and velocity boundary conditions, Whitehead & Doering (2011, 2012) recently used the background method to prove that $Nu \lesssim Ra^{5/12}$ uniformly in Pr for stress-free boundaries for steady or unsteady two-dimensional Rayleigh–Bénard convection (see also Otero 2002) and for three-dimensional Rayleigh–Bénard convection between stress-free boundaries at infinite Pr (see also Ierley, Kerswell & Plasting 2006).

As for the fixed energy problem, $Nu_{MAX}(Ra)$ obtained using the approach adopted in this paper has the same scaling in Ra as the upper bounds obtained using the background method. For fixed Γ, Chini & Cox (2009) analysed steady unicellular Rayleigh–Bénard convection and found that $Nu \sim Ra^{1/3}$, in agreement with the scaling of $Nu_{max}(Ra,\,\Gamma)$ with Ra observed here. This agreement suggests that steady Rayleigh–Bénard convection in pure fluids in a cell of fixed aspect ratio (and with stress-free boundaries) transports as much heat as any steady flow with a given amount of enstrophy, modulo a prefactor.

https://doi.org/10.1017/jfm.2014.306 Published online by Cambridge University Press

	$Nu(Ra, Pr)$	$Nu(Ra, \Gamma_{fixed})$
Classical theories		
Malkus (1954) and Howard (1964)	$\sim C\,Ra^{1/3}$	
Spiegel (1962) and Kraichnan (1962)	$\sim C\,(Pr\,Ra)^{1/2}$	
Background method (upper bounds)		
Ierley *et al.* (2006): numerical, infinite Pr	$\leqslant C\,Ra^{5/12}$	
Otero (2002): 2-D numerical, finite Pr	$\leqslant 0.142\,Ra^{5/12}$	
Whitehead & Doering (2011): analytical, 2-D finite Pr and 3-D infinite Pr	$\leqslant 0.289\,Ra^{5/12}$	
Steady unicellular analysis		
Chini & Cox (2009): asymptotic, finite Pr		$\sim C(\Gamma)\,Ra^{1/3}$
Current work		
Numerical	$\leqslant 1 + 0.115\,Ra^{5/12}$	$\leqslant 1 + (K(\Gamma))^{4/3}\,Ra^{1/3}$

TABLE 2. Comparison of the results of the current work with the scalings for Rayleigh–Bénard convection in pure fluids with stress-free boundary conditions obtained using various other methods.

5. Summary and discussions

In this work we have addressed some fundamental problems in fluid mechanics, namely how much heat can be transported between impermeable fixed temperature walls by steady incompressible flows with a given amount of kinetic energy or enstrophy, and what the optimal flows look like. We employed the calculus of variations to find flows that maximize the heat transport between the walls, answering the above questions for steady two-dimensional flows with, in the fixed enstrophy case, stress-free walls. For small energy or enstrophy, the resulting nonlinear Euler–Lagrange equations were linearized and solved analytically, revealing that the optimal flows are arrays of convection cells. For larger energy or enstrophy budgets, we solved the Euler–Lagrange equations using numerical continuation in a cell of a given aspect ratio Γ. For the problem with fixed kinetic energy, we were able to exploit the symmetries of the optimal flow to analytically solve the fully nonlinear equations using matched asymptotic analysis. The analytical and numerical results agree remarkably well. Our results are presented in terms of the Nusselt number Nu and the Péclect number Pe. We found that $Nu_{MAX} \sim Pe$ for the fixed energy problem and $Nu_{MAX} \sim Pe^{10/17}$ when the enstrophy is specified.

For each of the two primary flow-intensity constraints we have observed that there is a classical buoyancy-driven flow that satisfies the given constraint. We have thus interpreted our results in terms of the Rayleigh number Ra to see how the optimal transport compares with available upper bounds for Rayleigh–Bénard convection. In porous medium convection, which occurs at a mean energy fixed by Nu and Ra, we found that $Nu_{MAX} \sim Ra$ and $\Gamma_{opt} \sim Ra^{-1/2}$. For Rayleigh–Bénard convection in pure fluids, an example of fixed (mean) enstrophy transport, we found that $Nu_{MAX} \sim Ra^{5/12}$ and $\Gamma_{opt} \sim Ra^{-1/4}$. The Rayleigh-number scaling of the bounds on Nu agree with bounds derived by other methods for both problems, and also agree with the scaling found in the DNS of porous media convection in the high-Ra regime. Interestingly, for both problems, the scalings of $\Gamma_{opt}(Ra)$ found here agree with the scalings of the shortest-wavelength unstable mode about the linear conduction profile (see also Wen *et al.* 2012).

https://doi.org/10.1017/jfm.2014.306 Published online by Cambridge University Press

The results presented here offer new insights into steady optimal transport in two spatial dimensions, but several lines of research remain to be pursued to complete our understanding of the limits on fluid dynamical transport between impermeable walls. For example, the fixed enstrophy problem with no-slip boundary conditions is more challenging but of greater applicability for many applications and for laboratory experiments. Indeed, the best known rigorous bound for arbitrary-Prandtl-number Rayleigh–Bénard convection between no-slip boundaries is $Nu \lesssim Ra^{1/2}$ (Howard 1963; Doering & Constantin 1996; Plasting & Kerswell 2003), corresponding to $Nu \sim Pe^{2/3}$, but we do not know whether this estimate is sharp. Note that $2/3 > 10/17$, which leaves open the possibility that flow between no-slip boundaries may transport more than flow between stress-free walls at the same bulk enstrophy level. It is also natural to wonder if optimal transport in three dimensions takes place by three-dimensional flows. Finally, it is necessary to determine whether the true optimal transport is realized by time-dependent, rather than steady, flows. Unsteady optimal transport can be framed in the language of optimal control theory, producing new challenges for both analytical and computational investigations.

Acknowledgements

Much of this work was completed at the 2012 Geophysical Fluid Dynamics (GFD) Program at Woods Hole Oceanographic Institution. The GFD Program is supported by the US National Science Foundation (NSF) award OCE-0824636 and the Office of Naval Research. The Computational Fluid Dynamics Laboratory and the Department of Mechanical Engineering of UC Berkeley provided computational resources. This work was also supported by NASA awards NXX10AB93G and NXX13AG56G (to P.H.) and NSF awards AST-1010046 and AST-1009907 (to P.H.), PHY-0855335, DMS-0927587 and PHY-1205219 (to C.R.D.) and DMS-0928098 (to G.P.C.). We gratefully acknowledge helpful discussions with Cédric Beaume, Lindsey Corson, Duncan Hewitt, Genta Kawahara, Phil Marcus and Felix Otto.

Appendix A. Equations for the Newton–Kantorovich iteration scheme

First we rewrite (3.33)–(3.35) as

$$\Delta\psi = F(\theta_x, \theta_z, \phi_x, \phi_z), \tag{A 1}$$

$$\Delta\theta = G(\psi_x, \psi_z, \theta_x, \theta_z), \tag{A 2}$$

$$\Delta\phi = Q(\psi_x, \psi_z, \phi_x, \phi_z), \tag{A 3}$$

where

$$F = \frac{1}{\mu}\big(-(1+\phi_z)\theta_x + (\theta_z - 1)\phi_x\big), \tag{A 4}$$

$$G = (1-\theta_z)\psi_x + \psi_z\theta_x, \tag{A 5}$$

$$Q = (1+\phi_z)\psi_x - \psi_z\phi_x. \tag{A 6}$$

Taylor expanding the nonlinear terms F, G and Q about the solution of the Nth iteration gives

$$\Delta\psi^{N+1} = F^N + \delta\theta_x F^N_{\theta_x} + \delta\theta_z F^N_{\theta_z} + \delta\phi_x F^N_{\phi_x} + \delta\phi_z F^N_{\phi_z} + \text{h.o.t}, \tag{A 7}$$

$$\Delta\theta^{N+1} = G^N + \delta\psi_x G^N_{\psi_x} + \delta\psi_z G^N_{\psi_z} + \delta\theta_x G^N_{\theta_x} + \delta\theta_z G^N_{\theta_z} + \text{h.o.t}, \tag{A 8}$$

$$\Delta\phi^{N+1} = Q^N + \delta\psi_x Q^N_{\psi_x} + \delta\psi_z Q^N_{\psi_z} + \delta\phi_x Q^N_{\phi_x} + \delta\phi_z Q^N_{\phi_z} + \text{h.o.t}, \tag{A 9}$$

where subscripts of F, G and Q denote Frechet derivatives (e.g. $F_{\psi_x} \equiv \partial F/\partial\psi_x$) and

https://doi.org/10.1017/jfm.2014.306 Published online by Cambridge University Press

a superscript N means that the quantity is evaluated at iteration N. A 'δ' in front of any quantity means the difference between its values at iterations $N+1$ and N (e.g. $\delta\psi \equiv \psi^{N+1} - \psi^N$). The higher-order terms (h.o.t) are $O((\delta(\cdot))^2)$ or smaller.

After calculating the Frechet derivatives and ignoring higher-order terms, (A 7)–(A 9) become

$$\begin{aligned}
&\mu\Delta\delta\psi + (1+\phi_z^N)\,\delta\theta_x - \phi_x^N\,\delta\theta_z + (1-\theta_z^N)\,\delta\phi_x + \theta_x^N\,\delta\phi_z \\
&\quad = -\mu\Delta\psi^N - \left[(1+\phi_z^N)\theta_x^N + (1-\theta_z^N)\phi_x^N\right], \qquad \text{(A 10)}\\
&\Delta\delta\theta - \psi_z^N\,\delta\theta_x + \psi_x^N\,\delta\theta_z - (1-\theta_z^N)\,\delta\psi_x - \theta_x^N\,\delta\psi_z \\
&\quad = -\Delta\theta^N + (1-\theta_z^N)\psi_x^N + \psi_z^N\theta_x^N, \qquad \text{(A 11)}\\
&\Delta\delta\phi - (1+\phi_z^N)\,\delta\psi_x + \phi_x^N\,\delta\psi_z + \psi_z^N\,\delta\phi_x - \psi_x^N\,\delta\phi_z \\
&\quad = -\Delta\phi^N + (1+\phi_z^N)\psi_x^N - \psi_z^N\phi_x^N. \qquad \text{(A 12)}
\end{aligned}$$

Appendix B. Small-*Pe* solution for the fixed enstrophy problem

Fourier transforming (4.20) and (4.22) in the x direction yields

$$\begin{aligned}
(\mathrm{D}_z^2 - k^2)\,\hat{\theta}_k(z) + \hat{w}_k(z) &= 0, \qquad \text{(B 1)}\\
-\mu(\mathrm{D}_z^2 - k^2)^2\,\hat{w}_k(z) + 2k^2\,\hat{\theta}_k(z) &= 0, \qquad \text{(B 2)}
\end{aligned}$$

with solutions of the form

$$\begin{aligned}
\hat{w}_k(z) &= A_k \sin(m\pi z), \qquad \text{(B 3)}\\
\hat{\theta}_k(z) &= B_k \sin(m\pi z). \qquad \text{(B 4)}
\end{aligned}$$

Substitution into (B 1) and (B 2) gives

$$\begin{aligned}
\mu &= (2k^2)/(m^2\pi^2 + k^2)^3, \qquad \text{(B 5)}\\
A_k &= (m^2\pi^2 + k^2)\,B_k. \qquad \text{(B 6)}
\end{aligned}$$

Then (4.21) yields

$$\hat{u}_k(z) = \mathrm{i}\,\frac{m\pi}{k}\,A_k \cos(m\pi z). \qquad \text{(B 7)}$$

Substituting (B 7) and (B 3) into (4.12) gives

$$\left\langle |\boldsymbol{\nabla v}|^2 \right\rangle = \frac{1}{k^2}\left(m^2\pi^2 + k^2\right)^2 A_k^2 = Pe^2 \implies A_k = \frac{k}{(m^2\pi^2 + k^2)}\,Pe, \qquad \text{(B 8)}$$

which, combined with (B 6), yields

$$B_k = \frac{k}{(m^2\pi^2 + k^2)^2}\,Pe. \qquad \text{(B 9)}$$

The Nusselt number follows from (2.15):

$$Nu = 1 + A_k B_k = 1 + \frac{k^2}{(m^2\pi^2 + k^2)^3}\,Pe^2. \qquad \text{(B 10)}$$

Appendix C. Interior solution for the fixed enstrophy problem

Equations (4.26)–(4.29) can be written in terms of (ψ, ξ, η) as follows:

https://doi.org/10.1017/jfm.2014.306 Published online by Cambridge University Press

$$-\mathrm{J}(\xi,\eta)-2\mu\Delta^2\psi+2\xi_x=0, \tag{C 1}$$

$$\mathrm{J}(\psi,\xi)+\Delta\eta=0, \tag{C 2}$$

$$\mathrm{J}(\psi,\eta)+\Delta\xi-2\psi_x=0, \tag{C 3}$$

which are the same as (3.44)–(3.46) except that $+2\mu\Delta$ has been replaced by $-2\mu\Delta^2$. However, the higher-order derivative is expected to result in significant differences between the two problems.

The numerical results suggest that

$$\psi = \bar{\psi}(x)\,A(x,z), \tag{C 4}$$

$$\xi = \bar{\xi}(x)\,B(x,z), \tag{C 5}$$

$$\eta = \bar{\eta}(z)\,C(x,z), \tag{C 6}$$

where $(\bar{\psi},\bar{\xi},\bar{\eta})$ constitute the outer solution.

Using $(\bar{\psi}(x),\ \bar{\xi}(x),\ \bar{\eta}(z))$ in (C 1)–(C 3) gives

$$2\mu\,\bar{\psi}_{xxxx}-(2-\bar{\eta}_z)\,\bar{\xi}_x=0, \tag{C 7}$$

$$\bar{\eta}_{zz}=0, \tag{C 8}$$

$$\bar{\xi}_{xx}-(2-\bar{\eta}_z)\bar{\psi}_x=0, \tag{C 9}$$

which again implies that

$$\bar{\eta}(z)=\bar{\eta}_o\,z, \tag{C 10}$$

where $\bar{\eta}_o$ is an unknown constant. Eliminating $\bar{\psi}$ between (C 7) and (C 9) yields

$$\bar{\xi}_{xxxxx}-\left(\frac{\bar{\eta}_o-2}{\sqrt{2\mu}}\right)^2\bar{\xi}_x=0. \tag{C 11}$$

Given the periodicity of 2Γ in x and the fact that $\xi_x(\pm\Gamma/2,z)=0$, this implies that

$$\bar{\xi} = \pm\bar{\xi}_o\sin(\pi x/\Gamma), \tag{C 12}$$

$$\bar{\eta}_o = 2-\left(\frac{\pi}{\Gamma}\right)^2\sqrt{2\mu}, \tag{C 13}$$

where $\bar{\xi}_o>0$ is an unknown constant. Notice the difference between (C 13) and (3.56).

Equation (C 9) yields

$$\bar{\psi}=\frac{\pm\bar{\xi}_o}{(\pi/\Gamma)\sqrt{2\mu}}\cos(\pi x/\Gamma). \tag{C 14}$$

As before, the interior flow field (i.e. the outer solution) is known up to an unknown constant $\bar{\xi}_o$, which is to be determined using the inner solution.

REFERENCES

BOYD, J. P. 2001 *Chebyshev and Fourier Spectral Methods*, 2nd edn. Dover.

BUSSE, F. H. 1969 On Howard's bound for heat transport by turbulent convection. *J. Fluid Mech.* **37**, 457–477.

BUSSE, F. H. 1970 Bounds for turbulent shear flow. *J. Fluid Mech.* **41**, 219–240.

https://doi.org/10.1017/jfm.2014.306 Published online by Cambridge University Press

BUSSE, F. H. & JOSEPH, D. D. 1972 Bounds for heat transport in a porous layer. *J. Fluid Mech.* **54**, 521–543.

CAULFIELD, C. P. & KERSWELL, R. R. 2001 Maximal mixing rate in turbulent stably stratified Couette flow. *Phys. Fluids* **13**, 894–900.

CHESKIDOV, A., PETROV, N. P. & DOERING, C. R. 2007 Energy dissipation in fractal-forced flow. *J. Math. Phys.* **48**, 065208.

CHINI, G. P. & COX, S. M. 2009 Large Rayleigh number thermal convection: heat flux predictions and strongly nonlinear solutions. *Phys. Fluids* **21** (8), 083603.

CORSON, L. T. 2011 Maximizing the heat flux in steady unicellular porous media convection. *Tech. Rep.*, Geophysical Fluid Dynamics Program. Woods Hole Oceanographic Institution.

CORTELEZZI, L., ADROVER, A. & GIONA, M. 2008 Feasibility, efficiency and transportability of short horizon optimal mixing protocols. *J. Fluid Mech.* **597**, 199–231.

D'ALESSANDRO, D., DAHLEH, M. & MEZIC, I. 1999 Control of mixing in fluid flow: a maximum entropy approach. *IEEE Trans. Autom. Control* **44** (10), 1852–1863.

DOERING, C. R. & CONSTANTIN, P. 1992 Energy dissipation in shear driven turbulence. *Phys. Rev. Lett.* **69**, 1648–1651.

DOERING, C. R. & CONSTANTIN, P. 1994 Variational bounds on energy dissipation in incompressible flows: shear flow. *Phys. Rev.* E **49**, 4087–4099.

DOERING, C. R. & CONSTANTIN, P. 1996 Variational bounds on energy dissipation in incompressible flows. III. Convection. *Phys. Rev.* E **53**, 5957–5981.

DOERING, C. R. & CONSTANTIN, P. 1998 Bounds for heat transport in a porous layer. *J. Fluid Mech.* **376**, 263–296.

DOERING, C. R., ECKHARDT, B. & SCHUMACHER, J. 2003 Energy dissipation in body-forced plane shear flow. *J. Fluid Mech.* **494**, 275–284.

DOERING, C. R. & FOIAS, C. 2002 Energy dissipation in body-forced turbulence. *J. Fluid Mech.* **467**, 289–306.

DOERING, C. R., OTTO, F. & REZNIKOFF, M. G. 2006 Bounds on vertical heat transport for infinite-Prandtl-number Rayleigh–Bénard convection. *J. Fluid Mech.* **560**, 229–241.

DOERING, C. R., SPIEGEL, E. A. & WORTHING, R. A. 2000 Energy dissipation in a shear layer with suction. *Phys. Fluids* **12**, 1955–1968.

DRAZIN, P. G. & REID, W. H. 2004 *Hydrodynamic Stability*, 2nd edn. Cambridge University Press.

FOWLER, A. C. 1997 *Mathematical Models in the Applied Sciences*. Cambridge University Press.

GUBANOV, O. & CORTELEZZI, L. 2010 Towards the design of an optimal mixer. *J. Fluid Mech.* **651**, 27–53.

GUBANOV, O. & CORTELEZZI, L. 2012 On the cost efficiency of mixing optimization. *J. Fluid Mech.* **692**, 112–136.

GUPTA, V. P. & JOSEPH, D. D. 1973 Bounds for heat transport in a porous layer. *J. Fluid Mech.* **57**, 491–514.

HAGSTROM, G. & DOERING, C. R. 2010 Bounds on heat transport in Bénard–Marangoni convection. *Phys. Rev.* E **81**, 047301.

HAGSTROM, G. I. & DOERING, C. R. 2014 Bounds on surface stress-driven shear flow. *J. Nonlinear Sci.* **24**, 185–199.

HASSANZADEH, P. 2012 Optimal transport from wall to wall. Master's thesis, University of California, Berkeley.

HEWITT, D. R., NEUFELD, J. A. & LISTER, J. R. 2012 Ultimate regime of high Rayleigh number convection in a porous medium. *Phys. Rev. Lett.* **108** (22), 224503.

HEWITT, D. R., NEUFELD, J. A. & LISTER, J. R. 2013 Stability of columnar convection in a porous medium. *J. Fluid Mech.* **737**, 205–231.

HORNE, R. N. & O'SULLIVAN, P. 1978 Origin of oscillatory convection in a porous medium heated from below. *Phys. Fluids* **21**, 1260–1264.

HOWARD, L. N. 1963 Heat transport by turbulent convection. *J. Fluid Mech.* **17**, 405–432.

HOWARD, L. 1964 Convection at high Rayleigh numbers. In *Proceedings of the 11th International Congress of Applied Mechanics* (ed. H. Görtler) pp. 1109–1115. Springer.

https://doi.org/10.1017/jfm.2014.306 Published online by Cambridge University Press

IERLEY, G. R., KERSWELL, R. R. & PLASTING, S. C. 2006 Infinite-Prandtl-number convection. Part 2. A singular limit of upper bound theory. *J. Fluid Mech.* **560**, 159–228.

KERSWELL, R. R. 1996 Upper bounds on the energy dissipation in turbulent precession. *J. Fluid Mech.* **321**, 335–370.

KERSWELL, R. R. 1998 Unification of variational principles for turbulent shear flows: the background method of Doering–Constantin and the mean-fluctuation formulation of Howard–Busse. *Physica* D **121**, 175–192.

KRAICHNAN, R. H. 1962 Turbulent thermal convection at arbitrary Prandtl number. *Phys. Fluids* **5**, 1374–1389.

KROMMES, J. A. & SMITH, R. A. 1987 Rigorous upper bounds for transport due to passive advection by inhomogeneous turbulence. *Ann. Phys.* **177**, 246–329.

LIN, Z., THIFFEAULT, J.-L. & DOERING, C. R. 2011 Optimal stirring strategies for passive scalar mixing. *J. Fluid Mech.* **675**, 465–476.

MALKUS, W. V. R. 1954 The heat transport and spectrum of thermal turbulence. *Proc. R. Soc. Lond. Ser.* A **225**, 196–212.

MATHEW, G., MEZIC, I., GRIVOPOULOS, S., VAIDYA, U. & PETZOLD, L. 2007 Optimal control of mixing in Stokes fluid flows. *J. Fluid Mech.* **580**, 261–281.

NICKERSON, E. C. 1969 Upper bounds on torque in cylindrical Couette flow. *J. Fluid Mech.* **38**, 807–815.

OKABE, T., ECKHARDT, B., THIFFEAULT, J.-L. & DOERING, C. R. 2008 Mixing effectiveness depends on the source-sink structure: simulation results. *J. Stat. Mech. Theor. Exp.* **07**, P07018.

OTERO, J. 2002. Bounds for the heat transport in turbulent convection. PhD thesis, University of Michigan, Ann Arbor.

OTERO, J., DONTCHEVA, L. A., JOHNSTON, H., WORTHING, R. A., KURGANOV, A., PETROVA, G. & DOERING, C. R. 2004 High-Rayleigh-number convection in a fluid-saturated porous layer. *J. Fluid Mech.* **500**, 263–281.

PETROV, N. P., LU, L. & DOERING, C. R. 2005 Variational bounds on the energy dissipation rate in body-forced shear flow. *J. Turbul.* **6**, 17.

PLASTING, S. C. & KERSWELL, R. R. 2003 Improved upper bound on the energy dissipation rate in plane Couette flow: the full solution to Busse's problem and the Constantin–Doering–Hopf problem with one-dimensional background field. *J. Fluid Mech.* **477**, 363–379.

PLASTING, S. C. & YOUNG, W. R. 2006 A bound on scalar variance for the advection–diffusion equation. *J. Fluid Mech.* **552**, 289–298.

RAYLEIGH, L. 1916 On convection currents in a horizontal layer of fluid, when the higher temperature is on the under side. *Phil. Mag.* **32**, 529–546.

ROLLIN, B., DUBIEF, Y. & DOERING, C. R. 2011 Variations on Kolmogorov flow: turbulent energy dissipation and mean flow profiles. *J. Fluid Mech.* **670**, 204–213.

SHAW, T. A., THIFFEAULT, J.-L. & DOERING, C. R. 2007 Stirring up trouble: multi-scale mixing measures for steady scalar sources. *Physica* D **231**, 143–164.

SIGGERS, J. H., KERSWELL, R. R. & BALMFORTH, N. J. 2004 Bounds on horizontal convection. *J. Fluid Mech.* **517**, 55–70.

SPIEGEL, E. A. 1962 Thermal turbulence at very small Prandtl number. *J. Geophys. Res.* **67**, 3063–3070.

TANG, W., CAULFIELD, C. P. & KERSWELL, R. R. 2009 A prediction for the optimal stratification for turbulent mixing. *J. Fluid Mech.* **634**, 487–497.

TANG, W., CAULFIELD, C. P. & YOUNG, W. R. 2004 Bounds on dissipation in stress driven flow. *J. Fluid Mech.* **510**, 333–352.

THIFFEAULT, J.-L., DOERING, C. R. & GIBBON, J. D. 2004 A bound on mixing efficiency for the advection–diffusion equation. *J. Fluid Mech.* **521**, 105–114.

TREFETHEN, L. N. 2001 *Spectral Methods in MATLAB*. Society for Industrial and Applied Mathematics.

WEN, B., CHINI, G. P., DIANATI, N. & DOERING, C. R. 2013 Computational approaches to aspect-ratio-dependent upper bounds and heat flux in porous medium convection. *Phys. Lett.* A **377**, 2931–2938.

https://doi.org/10.1017/jfm.2014.306 Published online by Cambridge University Press

WEN, B., DIANATI, N., LUNASIN, E., CHINI, G. P. & DOERING, C. R. 2012 New upper bounds and reduced dynamical modelling for Rayleigh–Bénard convection in a fluid saturated porous layer. *Commun. Nonlinear Sci. Numer. Simul.* **17**, 2191–2199.

WHITEHEAD, J. P. & DOERING, C. R. 2011 Ultimate state of two-dimensional Rayleigh–Bénard convection between free-slip fixed-temperature boundaries. *Phys. Rev. Lett.* **106**, 244501.

WHITEHEAD, J. P. & DOERING, C. R. 2012 Rigid bounds on heat transport by a fluid between slippery boundaries. *J. Fluid Mech.* **707**, 241–259.

https://doi.org/10.1017/jfm.2014.306 Published online by Cambridge University Press